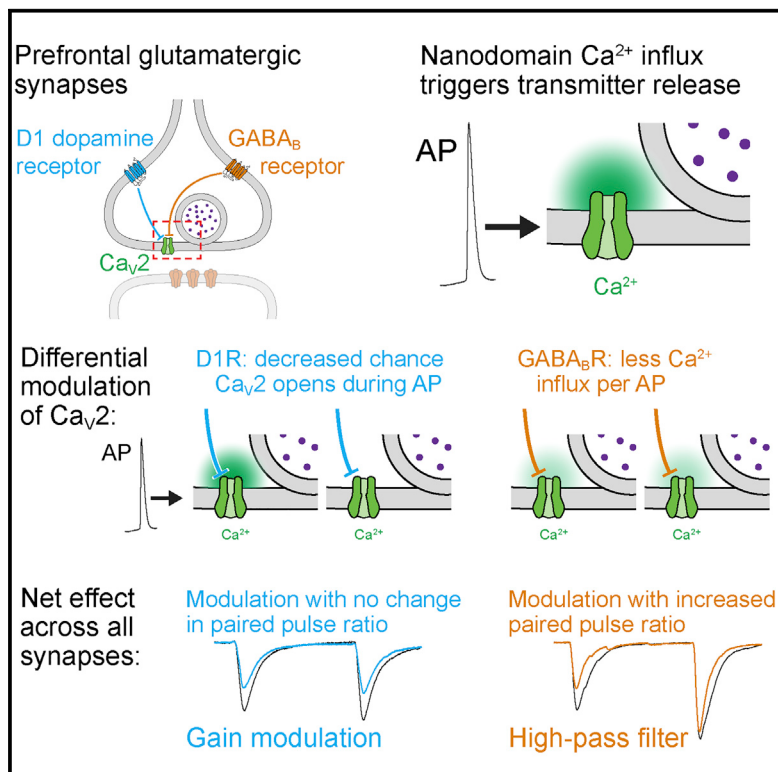


## Two Forms of Synaptic Depression Produced by Differential Neuromodulation of Presynaptic Calcium Channels

### Graphical Abstract



### Authors

Kenneth J. Burke, Jr.,  
Caroline M. Keeshen, Kevin J. Bender

### Correspondence

kevin.bender@ucsf.edu

### In Brief

Presynaptic neuromodulators like GABA<sub>B</sub> receptors impose high-pass filters on synaptic transmission, facilitating release when inputs arrive at high frequency. Burke et al. show that, unlike GABA<sub>B</sub>, dopamine suppresses glutamatergic release in prefrontal cortex independent of frequency, thus regulating synaptic gain.

### Highlights

- Dopamine suppresses specific glutamatergic inputs to prefrontal cortex
- This presynaptic suppression occurs without increasing short-term facilitation
- GABA<sub>B</sub> receptors increase facilitation at the same synapse
- Biased regulation of presynaptic calcium channels underlies these differences



# Two Forms of Synaptic Depression Produced by Differential Neuromodulation of Presynaptic Calcium Channels

Kenneth J. Burke, Jr.,<sup>1</sup> Caroline M. Keeshen,<sup>2</sup> and Kevin J. Bender<sup>1,2,3,\*</sup>

<sup>1</sup>Neuroscience Graduate Program

<sup>2</sup>Weill Institute for Neurosciences

Department of Neurology, University of California, San Francisco, San Francisco, CA, USA

<sup>3</sup>Lead Contact

\*Correspondence: kevin.bender@ucsf.edu

<https://doi.org/10.1016/j.neuron.2018.07.030>

## SUMMARY

Neuromodulators are important regulators of synaptic transmission throughout the brain. At the presynaptic terminal, neuromodulation of calcium channels (CaVs) can affect transmission not only by changing neurotransmitter release probability, but also by shaping short-term plasticity (STP). Indeed, changes in STP are often considered a requirement for defining a presynaptic site of action. Nevertheless, some synapses exhibit non-canonical forms of neuromodulation, where release probability is altered without a corresponding change in STP. Here, we identify biophysical mechanisms whereby both canonical and non-canonical presynaptic neuromodulation can occur at the same synapse. At a subset of glutamatergic terminals in prefrontal cortex, GABA<sub>B</sub> and D1/D5 dopamine receptors suppress release probability with and without canonical increases in short-term facilitation by modulating different aspects of presynaptic CaV function. These findings establish a framework whereby signaling from multiple neuromodulators can converge on presynaptic CaVs to differentially tune release dynamics at the same synapse.

## INTRODUCTION

Neuromodulators regulate synaptic transmission through a wide array of biophysical mechanisms (Chalifoux and Carter, 2011; Seamans and Yang, 2004; Tritsch and Sabatini, 2012). In presynaptic boutons, neuromodulators can affect the function of voltage-gated calcium channels (CaVs), which in turn alters the probability of vesicle release ( $P_R$ ) (Branco and Staras, 2009). Due to complex interactions between calcium (Ca) influx and vesicle release machinery in the presynaptic active zone, changes in  $P_R$  typically do not result in a simple change in gain (i.e., a linear scaling of synaptic strength). Canonically, presynaptic modulators change the relative strength of subsequent closely timed synaptic events, a phenomenon termed short-

term plasticity (STP) (Kamiya and Zucker, 1994; Zucker and Regehr, 2002; Hennig, 2013; Jackman and Regehr, 2017). However, exceptions to this rule have been observed for a variety of neuromodulators and synapses. In these instances, presynaptic modulation suppresses  $P_R$  without canonical changes in STP (Gao et al., 2001; Seamans et al., 2001; Delaney et al., 2007; Li et al., 2012; Holmes et al., 2017; Tejeda et al., 2017). Moreover, modulation with and without parallel changes in STP has been observed at a single synapse in response to two different neuromodulators (Heft et al., 2002; Delaney et al., 2007; Li et al., 2012; Tejeda et al., 2017). Why this occurs at some synapses and why different neuromodulators evoke different forms of presynaptic suppression are unclear.

In prefrontal cortex (PFC), there is evidence that GABA and dopamine may differentially regulate glutamatergic transmission by activating presynaptic GABA<sub>B</sub> receptors (GABA<sub>B</sub>R) and D1/D5 family dopamine receptors (D1R). At these synapses, GABA<sub>B</sub>R activation acts as a canonical presynaptic neuromodulator, robustly reducing  $P_R$  for single presynaptic action potentials (APs) but facilitating later events in a high-frequency burst of APs (Chalifoux and Carter, 2011). As such, GABA<sub>B</sub>R activation is thought to impose a high-pass filter on these synapses (Abbott and Regehr, 2004). How dopamine regulates the same synapses is less clear. Dopamine modestly suppresses glutamatergic excitatory postsynaptic currents when excitatory postsynaptic currents (EPSCs) are evoked by local electrical stimulation (Seamans et al., 2001; Urban et al., 2002). By contrast, EPSCs between synaptically coupled pairs of glutamatergic neurons are more strongly suppressed, suggesting that dopamine may suppress presynaptic release in an input-specific manner (Gao et al., 2001, 2003; Gao and Goldman-Rakic, 2002; but see Urban et al., 2002). Although other lines of evidence suggest a presynaptic site of action, this modulation occurs without a change in STP (Gao et al., 2001; Seamans et al., 2001). Thus, in contrast to GABA<sub>B</sub>, dopamine may act non-canonically to regulate presynaptic gain. This may be important for the hypothesized role of D1R in suppressing background noise during working memory tasks *in vivo* (Vijayraghavan et al., 2007).

Using a combination of pharmacology, two-photon Ca imaging, and computational modeling, we found that activation of either D1R or GABA<sub>B</sub>R suppressed  $P_R$ , but with differential effects on short-term dynamics. We examined D1R modulation at a variety of glutamatergic inputs to PFC and found that D1R



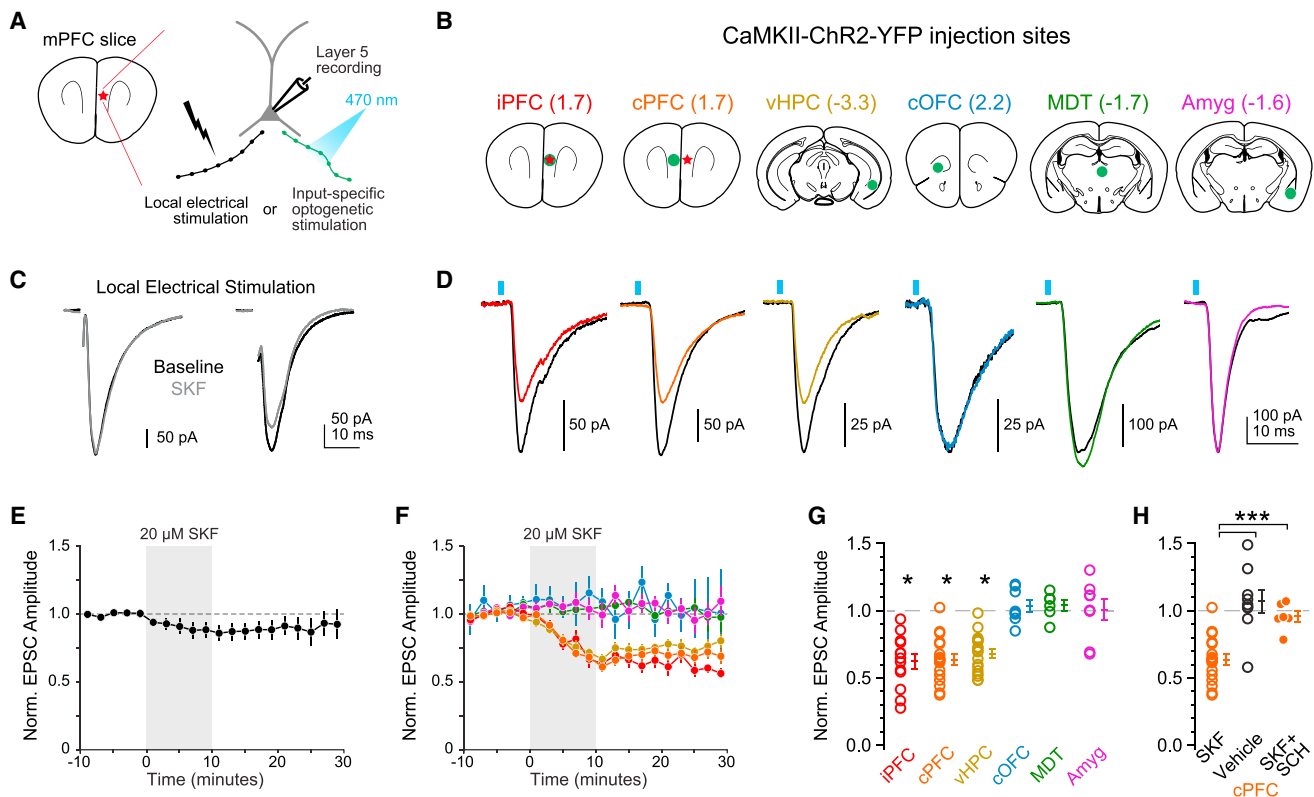


**Figure 1. D1R Suppresses a Subset of Excitatory Synapses in PFC**

(A) Schematics of *in vitro* recording location in mPFC (left) and stimulation configurations (right). EPSC currents were evoked via local theta-barrel electrode or by input-specific ChR2 stimulation.

(B) ChR2-expressing virus injection locations, with injection sites shown in green and recording site in red where applicable. Numbers in parenthesis are distance from bregma (mm).

(C) Representative effects of D1R activation on electrode-evoked eEPSCs. Baseline, black; post-SKF, gray.

(D) Same as (C), but for oEPSCs. Baseline, black; post-SKF, other colors.

(E and F) Summary of normalized EPSC amplitude over time for both eEPSC and oEPSC conditions (color coding as in (B)–(D)).

(G) Summary of change in EPSC after D1R activation (same cells as in F).

(H) Modulation of cPFC oEPSCs with vehicle or D1R activation in presence of D1R antagonist SCH23390.

suppressed glutamatergic transmission at only a subset of inputs, but did so with no increase in short-term facilitation. At synapses where D1R-mediated suppression was present, GABA<sub>B</sub>R activation also suppressed vesicular  $P_R$  but with canonical increases in short-term facilitation. At these synapses, we show that release is likely mediated by a very small number of CaVs and that these CaVs are the targets of both D1R and GABA<sub>B</sub>R signaling. Interestingly, D1R and GABA<sub>B</sub>R regulate different biophysical properties of presynaptic CaVs, which alone were sufficient to account for the differences in STP. Thus, the interplay between CaV function and vesicle release machinery, combined with the precise mechanism by which CaVs are regulated, can bias how neuromodulators regulate synaptic transmission.

## RESULTS

### Dopaminergic Modulation of Glutamatergic Inputs to PFC

To test the sensitivity of specific PFC excitatory inputs to dopaminergic modulation, we made whole-cell recordings from pyra-

midal cells in layer 5b of PFC and evoked EPSCs either via local electrical stimulation (eEPSC), which recruits an unknown population of inputs, or via optogenetic recruitment of anatomically specified inputs (oEPSC; Figures 1A and 1B). Stimuli were delivered every 15 s, and resulting EPSCs were monitored in cells voltage-clamped to  $-80$  mV. EPSCs were almost entirely blocked by the AMPA/kainate antagonist NBQX ( $10 \mu$ M; residual current =  $1.4\% \pm 0.8\%$  of baseline,  $n = 11$ ). Following a stable baseline, D1Rs were activated by application of the D1-selective agonist SKF 83822 ( $20 \mu$ M, with  $1 \mu$ M of the D2-family antagonist sulpiride present throughout recording). Consistent with previous findings (Seamans et al., 2001), eEPSCs evoked by local electrical stimulation were only modestly suppressed (Figures 1C and 1E; Norm Amp:  $0.88 \pm 0.05$  of baseline,  $n = 16$ ,  $p < 0.05$ ; rank-sum test). This suggests that dopamine has either minimal effects on all glutamatergic inputs to these neurons or perhaps selective effects depending on the input source.

To distinguish between these possibilities, we injected a virus encoding channelrhodopsin2 (ChR2) into six major glutamatergic input sources to mPFC (Figures 1B and S1; either

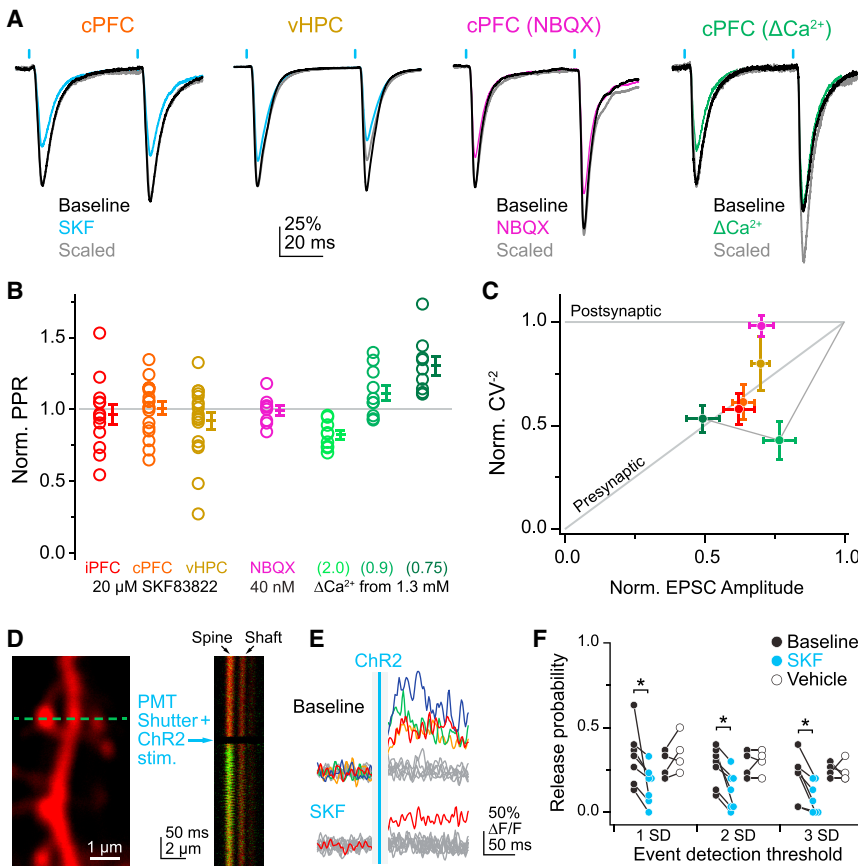


**Figure 2. D1R Modulates oEPSC Amplitude, Coefficient of Variation, and Release Probability but Not Paired-Pulse Ratio**

(A) Examples of D1R modulation of paired pulses. Baseline, black; post-SKF, cyan; post-SKF scaled, gray. From left to right: D1R activation of oEPSCs from cPFC and vHPC, subsaturating NBQX on cPFC oEPSCs (40 nM), and reduced extracellular calcium on cPFC oEPSCs. All traces scaled to baseline amplitude of first oEPSC for comparison.

(B) Summary of PPR change. Colors as in (A), with D1R activation of iPFC oEPSCs in red. All values normalized to pre-drug baseline, except  $\Delta\text{Ca}^{2+}$  conditions are normalized to PPR at 1.3 mM.

(C) Normalized CV plotted against change in oEPSC amplitude. Colors as in (B). Line connects green  $\Delta\text{Ca}^{2+}$  conditions in order of decreasing extracellular Ca concentration.

(D) Spine imaging configuration for OQA. Left: Example of Alexa 594 fluorescence in dendritic shaft and spines, with linescan location indicated by dashed blue line. Right: Example single-trial linescan of dendritic spine and shaft on left. PMTs were shuttered during LED stimulation. Note that shutter reopening resulted in a small amount of vibration, which is largely cancelled out when averaging fluorescence over the spine head area of the linescan.

(E) Trials before and after bath application of SKF. Data analyzed from Fluo-5F fluorescence only ( $\Delta\text{F/F}$ ). Gray and non-gray lines indicate failure and success trials, respectively. Blue vertical line is ChR2 timing.

(F) Changes in  $P_R$  with D1R stimulation or vehicle. All  $P_R$  measures are calculated as the ratio of successful trials to total trials. Different thresholds for defining a success trial are shown along the x axis.

AAV5-CaMKII $\alpha$ -ChR2-EYFP or AAV5-Ef1 $\alpha$ -DIO-ChR2-EYFP, see STAR Methods). Injections were made in PFC, both ipsilateral and contralateral to the recording site (iPFC, cPFC); ipsilateral ventral hippocampus (vHPC); contralateral orbitofrontal cortex (cOFC); ipsilateral mediodorsal thalamus (MDT); or ipsilateral amygdala (Amyg). In contrast to local electrical stimulation, optically evoked oEPSCs were modulated by SKF in only 3 of 6 inputs (Figures 1D, 1F, and 1G)—iPFC, cPFC, and vHPC (iPFC, Norm Amp:  $0.62 \pm 0.05$ , n = 13, p < 0.01; cPFC:  $0.64 \pm 0.04$ , n = 18, p < 0.01; vHPC:  $0.66 \pm 0.04$ , n = 18, p < 0.01; rank-sum test)—and were blocked by the D1 antagonist SCH 23390 (10  $\mu\text{M}$  SCH; Norm Amp:  $0.96 \pm 0.04$ , n = 6, p < 0.01 versus SKF alone; rank-sum test; Figure 1H). Inputs from cOFC, MDT, and Amyg were insensitive to D1 agonist application (cOFC, Norm Amp:  $1.03 \pm 0.04$ , n = 8, p = 0.47; MDT:  $1.04 \pm 0.04$ , n = 6, p = 0.37; Amyg:  $1.01 \pm 0.08$ , n = 8, p = 0.93; rank-sum test). Taken together, these data suggest that D1Rs suppress a subset of glutamatergic inputs into PFC that is defined, at least in part, by anatomical source.

The pattern of modulation observed above can be explained most easily by input-specific, presynaptic actions of D1Rs. To identify the locus of dopaminergic modulation, we first examined the paired-pulse ratio (PPR) and coefficient of variation (CV) of oEPSCs in modulated pathways. At many synapses, reductions

in  $P_R$  are accompanied by an increase in PPR and a decrease in  $\text{CV}^{-2}$ , whereas changes in postsynaptic charge transfer per vesicle lead to reductions in EPSC amplitude with no change in PPR or  $\text{CV}^{-2}$  (Clements, 1990; Kamiya and Zucker, 1994; Quastel, 1997; Sigworth, 1980). We first validated that PPR and CV accurately reflect changes to pre- and postsynaptic aspects of transmission by altering extracellular Ca concentration, which changes  $P_R$ , or by applying subsaturating concentrations of the AMPA/kainate receptor antagonist NBQX, which attenuates EPSC amplitude without altering  $P_R$ . These manipulations were calibrated to suppress the amplitude of the first oEPSC to a similar extent as observed after D1R activation. Neither PPR nor  $\text{CV}^{-2}$  was affected by NBQX application (40 nM), consistent with its postsynaptic actions (Norm Amp:  $0.70 \pm 0.04$ , p < 0.001; Norm PPR =  $0.99 \pm 0.04$ , p = 0.86; Norm  $\text{CV}^{-2}$ :  $0.98 \pm 0.05$ , p = 0.72; n = 8, rank-sum test). In contrast, both PPR and  $\text{CV}^{-2}$  co-varied with EPSC amplitude when extracellular Ca concentration was changed (Figures 2A–2C,  $\Delta\text{Ca}^{2+}$ ; relative to 1.3 mM  $\text{CaCl}_2$ . All data normalized to baseline. 2.0 mM, Amp:  $1.43 \pm 0.07$ , PPR =  $0.82 \pm 0.03$ ,  $\text{CV}^{-2} = 3.00 \pm 0.82$ , n = 9; 0.9 mM, Amp:  $0.77 \pm 0.06$ , PPR =  $1.11 \pm 0.05$ ,  $\text{CV}^{-2} = 0.43 \pm 0.09$ , n = 10; 0.75 mM, Amp:  $0.49 \pm 0.06$ , PPR =  $1.30 \pm 0.07$ ,  $\text{CV}^{-2} = 0.53 \pm 0.07$ , n = 9; PPR versus  $\text{Ca}^{2+}$ , chi-square statistic = 18.19, p < 0.001, Kruskal-Wallis; CV $^{-2}$  versus  $\text{Ca}^{2+}$ , chi-square

statistic = 18.22,  $p < 0.001$ , Kruskal-Wallis). Furthermore, baseline paired-pulse facilitation was comparable between the electrical and optical stimulation methods (for oEPSC, PPR = 1.38, 1.08–1.70 for median, 25<sup>th</sup>–75<sup>th</sup> percentile,  $n = 98$  cells; for eEPSC, PPR = 1.57, 1.27–1.83 for median, 25<sup>th</sup>–75<sup>th</sup> percentile,  $n = 16$ ;  $p = 0.12$ , rank-sum test). Taken together, this indicates that PPR and CV<sup>-2</sup> can distinguish between canonical pre- and postsynaptic manipulations at these synapses.

To examine how PPR is affected by D1Rs, oEPSCs were evoked in each dopamine-sensitive pathway. Comparable levels of paired-pulse facilitation were observed at baseline for iPFC, cPFC, and vHPC inputs ( $1.31 \pm 0.09$ ,  $1.31 \pm 0.08$ , and  $1.10 \pm 0.08$ , respectively; 50 ms interstimulus interval). Interestingly, PPR was not increased after D1-dependent modulation of iPFC, cPFC, or vHPC inputs (Figures 2A–2C, SKF, for iPFC, cPFC, and vHPC, respectively: Norm PPR =  $0.96 \pm 0.07$ ,  $1.01 \pm 0.04$ , and  $0.93 \pm 0.07$ ;  $n = 13$ , 18, and 18;  $p = 0.60$ , 0.83, and 0.20; rank-sum test with Holm-Sidak correction versus PPR = 1.00; chi-square statistic = 1.57,  $p = 0.67$ , Kruskal-Wallis), a result consistent with previous studies in PFC (Gao et al., 2001; Seamans et al., 2001). In contrast, CV<sup>-2</sup> was reduced at both prefrontal inputs and trended toward a decrease for ventral hippocampal inputs (iPFC, cPFC, and vHPC, respectively: Norm CV<sup>-2</sup> =  $0.58 \pm 0.07$ ,  $0.61 \pm 0.09$ , and  $0.82 \pm 0.10$ ;  $p = 0.0001$ ,  $p = 0.0003$ , and  $p = 0.107$ ).

Given the disagreement between PPR and CV results, we next sought to isolate pre- and postsynaptic components of synaptic transmission. To examine presynaptic  $P_R$ , we used optical quantal analysis (OQA), where transmission success and failure can be monitored at single synapses via NMDA receptor-mediated spine Ca influx (Mainen et al., 1999; Oertner et al., 2002; Higley et al., 2009; Little and Carter, 2012). Pyramidal cells were voltage-clamped to 0 mV to inactivate CaVs, and spines responsive to ChR2 stimuli were identified using Fluo-5F (Figures 2D–2F).  $P_R$  across all tested spines was  $0.28 \pm 0.03$  at baseline (range = 0.10–0.40,  $n = 11$  spines, 30 trials each). After pharmacological activation of D1Rs,  $P_R$  was significantly reduced (Figures 2E and 2F, success threshold = 2 SD of noise; baseline  $P_R = 0.27 \pm 0.04$ , post-SKF  $P_R = 0.13 \pm 0.04$ ,  $n = 7$ ,  $p < 0.05$ , signed-rank test).  $P_R$  was unaltered in time-locked controls (baseline  $P_R = 0.28 \pm 0.04$ , post-vehicle  $P_R = 0.30 \pm 0.04$ ,  $n = 4$ ,  $p > 0.99$ , signed-rank test). Data were consistent when using different noise thresholds to define success and failure trials (see STAR Methods; success threshold = 1 SD of noise; SKF baseline  $P_R = 0.33 \pm 0.06$ , post-SKF  $P_R = 0.16 \pm 0.04$ ,  $n = 7$ ,  $p < 0.05$ , vehicle baseline  $P_R = 0.28 \pm 0.04$ , post-vehicle  $P_R = 0.35 \pm 0.06$ ,  $n = 4$ ,  $p = 0.375$ ; success threshold = 3 SD of noise; SKF baseline  $P_R = 0.21 \pm 0.05$ , post-SKF  $P_R = 0.09 \pm 0.03$ ,  $n = 7$ ,  $p < 0.05$ , vehicle baseline  $P_R = 0.25 \pm 0.02$ , post-vehicle  $P_R = 0.24 \pm 0.03$ ,  $n = 4$ ,  $p > 0.99$ ). These data indicate that D1Rs suppress  $P_R$  at individual PFC synapses.

To isolate potential postsynaptic modulation by D1Rs, we bypassed transmitter release and instead uncaged glutamate on single spines. Uncaging pulses were delivered in a pair with increased intensity on the second pulse to mimic paired-pulse facilitation observed using ChR2 stimulation. No change in uEPSC amplitude or PPR was noted (Figure S4) (Norm uEPSC amplitude =  $1.01 \pm 0.11$  and  $0.97 \pm 0.06$ ,  $n = 8$  and 11 for SKF

and vehicle, respectively;  $p = 0.62$ , Mann-Whitney U test, SKF versus vehicle; Unnormalized PPR =  $1.45 \pm 0.21$ ,  $1.41 \pm 0.16$ ,  $1.41 \pm 0.10$ , and  $1.40 \pm 0.07$ ,  $n = 8$ , 8, 11, and 11 for SKF baseline, post-SKF, vehicle baseline, and post-vehicle, respectively;  $p = 0.87$ , Mann-Whitney U test for SKF baseline versus vehicle baseline;  $p > 0.99$ ,  $p = 0.86$ , Wilcoxon signed-rank test for baseline PPR versus post condition for SKF and vehicle, respectively).

D1 receptors are more commonly expressed in thin-tufted layer 5 pyramidal cells in PFC, which have intrinsic cell properties that can be distinguished from neighboring cell classes (Gee et al., 2012; Seong and Carter, 2012; Clarkson et al., 2017). To determine whether postsynaptic cell type contributes to D1-dependent modulation of oEPSCs, we divided the dataset from Figure 1 not by projection source but by postsynaptic cell class and found that D1R-dependent modulation was present in putative D1-expressing and D1-lacking cell classes (Figures S2C and S2D). Taken together with OQA and uncaging experiments, these data indicate that D1R suppression of long-range EPSCs is due to presynaptic suppression of  $P_R$ , despite the fact that this modulation does not increase PPR.

How might D1Rs suppress  $P_R$  without increasing paired-pulse facilitation? D1Rs have been observed to regulate the high-voltage-activated (HVA) CaVs that underlie transmitter release (Surmeier et al., 1995; Zhang et al., 2002; Seamans and Yang, 2004). To test whether D1Rs regulate presynaptic Ca influx, we imaged Ca in axonal boutons that originated from different long-range inputs using two-photon laser scanning microscopy. We used a viral strategy similar to that used with ChR2, injecting both AAV5-hSyn-DIO-gCaMP6f and AAV5-Ef1 $\alpha$ -Cre into the same brain regions as studied above in animals from a Cre-dependent tdTomato reporter line (Ai14; Figure 3A). In a subset of experiments, we confirmed that gCaMP6f responses were AP-mediated by visually ensuring that responses to a prolonged train of stimuli (50 $\times$  50 Hz, Figure 3A) were blocked by 1  $\mu$ M tetrodotoxin ( $n = 6$  boutons, 3 slices). When assessing D1R modulation, stimuli were limited to 3 $\times$  50 Hz, as this produced reliable gCaMP signals that were restricted to individual boutons (Figure S5, gCaMP full-width half-max  $1.70 \pm 0.16$   $\mu$ m before stimulus versus  $1.68 \pm 0.16$   $\mu$ m after stimulus,  $n = 8$ ,  $p = 0.88$ ; rank-sum test). Consistent with oEPSC results, D1R activation strongly suppressed AP-evoked Ca influx in axonal boutons from cPFC and vHPC, but not from cOFC, MDT, or Amyg (Figures 3B and 3C; Norm Peak  $\Delta F/F = 0.57 \pm 0.07$ ,  $0.71 \pm 0.08$ ,  $1.04 \pm 0.09$ ,  $1.01 \pm 0.11$ , and  $0.99 \pm 0.07$ ;  $n = 13$ , 12, 14, 13, and 10;  $p < 0.001$ ,  $p = 0.003$ ,  $p = 0.64$ ,  $p = 0.96$ , and  $p = 0.72$ , respectively; rank-sum test with Holm-Sidak correction), and modulation was blocked by SCH 23390 (10  $\mu$ M; Figure 3D; for SKF, Vehicle, and SKF+Sch, respectively: Norm Peak  $\Delta F/F = 0.57 \pm 0.07$ ,  $1.04 \pm 0.05$ , and  $1.03 \pm 0.08$ ;  $n = 13$ , 7, and 14; chi-square statistic = 14.80,  $p < 0.001$ , Kruskal-Wallis; SKF versus Vehicle  $p < 0.001$ , SKF versus SKF+Sch  $p < 0.001$ ; rank-sum test with Holm-Sidak correction). Note that iPFC boutons were not measured with this approach, as boutons could not be resolved within the dense fluorescence of the injection site. Instead, modulation at iPFC boutons was assessed by imaging axon Ca influx with synthetic indicators during whole-cell recordings (see Figure 4). Overall, these data suggest that D1Rs suppress specific PFC glutamatergic inputs by

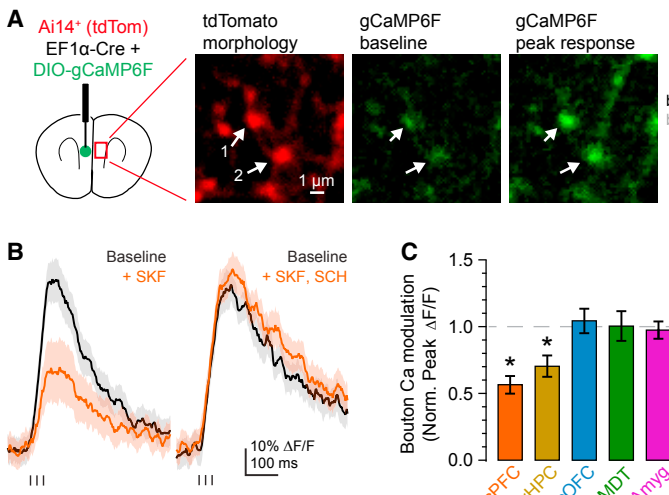


**Figure 3. D1R Suppresses Evoked Axonal Calcium Influx in PFC**

(A) Long-range axon imaging configuration. Left: Schematic of recording. Injection site in green, stimulation and imaging location in red box. Middle: Example fluorescence response of axonal boutons. Red fluorescence was used to locate boutons, green fluorescence was monitored in response to electrical stimulation. Arrows highlight two boutons quantified in right panel. Right: Normalized change in fluorescence for example boutons from middle panels.

(B) Evoked gCaMP6f signals in PFC boutons. SKF-mediated suppression was blocked by SCH23390. (C) Summary of change in peak ΔF/F in response to D1R activation for different long-range inputs to PFC (colors as in Figures 1 and 2). (D) Summary of modulation of peak ΔF/F responses from cPFC axonal boutons with vehicle application or D1R activation in presence of D1R antagonist SCH23390.

non-canonical presynaptic mechanism that reduces vesicle  $P_R$  without increasing paired-pulse facilitation.

### Canonical and Non-canonical Presynaptic Modulation at PFC Glutamatergic Inputs

Is dopamine unique in its ability to regulate  $P_R$  without altering STP, or do other presynaptic neuromodulators have similar effects at these synapses? To address this question, we compared the effects of D1R to GABA<sub>B</sub>R activation, which is known to suppress release through G<sub>βγ</sub>-dependent modulation of presynaptic CaVs (Chalifoux and Carter, 2011; Otis and Trussell, 1996; Park and Dunlap, 1998; Takahashi et al., 1998). The GABA<sub>B</sub>R agonist baclofen (350 nM) suppressed oEPSCs from cPFC inputs to a slightly larger extent than SKF (Figures 4A and 4B; Norm oEPSC Amp:  $0.46 \pm 0.05$ ,  $n = 7$ ,  $p < 0.001$ ; rank-sum test with Holm-Sidak correction; compare to Figures 1G and 1H); however, CV<sup>-2</sup> and PPR decreased and increased, respectively, to an extent that mimicked the reduced extracellular Ca condition (Figure 4B; Norm CV<sup>-2</sup>:  $0.39 \pm 0.08$ ,  $p < 0.001$ ; Norm PPR =  $1.27 \pm 0.10$ ,  $p = 0.03$ ; rank-sum test with Holm-Sidak correction; see also Figure S3). These data indicate that GABA<sub>B</sub>R-mediated suppression of presynaptic release leads to canonical increases in PPR, suggesting that neuromodulation by GABA<sub>B</sub>R and D1R may occur through different signaling mechanisms.

Previous work has shown that D1Rs, as opposed to G<sub>βγ</sub>-dependent GABA<sub>B</sub>Rs, regulate Ca<sub>v</sub>2.1 and Ca<sub>v</sub>2.2 CaVs through a protein kinase A-dependent (PKA) pathway (Surmeier et al., 1995; Zhang et al., 2002). To test this, as well as to measure neuromodulatory effects in iPFC axons, we made whole-cell recordings from layer 5 pyramidal cells and imaged AP-evoked bouton Ca transients with Fluo-5F. Ca transients were suppressed by SKF and baclofen to similar degrees (Figures 4C and 4D; Norm Peak ΔF/F =  $1.00 \pm 0.03$ ,  $0.56 \pm 0.06$ , and  $0.59 \pm 0.05$ ;  $n = 6$  each for vehicle, SKF, and baclofen, respectively), and Ca transients were suppressed by both D1R and GABA<sub>B</sub>R at individual boutons with serial application of both agonists (Norm Peak ΔF/F =  $0.62 \pm 0.03$  and  $0.44 \pm 0.05$  for SKF and SKF+baclofen, respectively;  $n = 7$ ,  $p < 0.05$ , signed-rank test). D1-dependent

modulation was blocked by the PKA inhibitor H89 (Figures 4C and 4D; Norm ΔF/F =  $0.98 \pm 0.02$ ,  $n = 8$ ), whereas GABA<sub>B</sub>R-dependent modulation was not (Norm ΔF/F =  $0.66 \pm 0.05$ ,  $n = 7$ ; chi-square statistic = 24.1,  $p < 0.001$ , Kruskal-Wallis; SKF versus SKF+H89  $p < 0.001$ , SKF versus Vehicle  $p = 0.002$ , baclofen versus baclofen+H89  $p = 0.366$ , baclofen versus Vehicle  $p = 0.002$ , baclofen+H89 versus Vehicle  $p = 0.001$ ; rank-sum test with Holm-Sidak correction).

We next tested whether the distinct signaling pathways of D1R and GABA<sub>B</sub>R result in regulation of different presynaptic CaV subtypes. Application of ω-conotoxin-MVIIC (1 μM) blocked oEPSCs by  $98.3\% \pm 0.6\%$  ( $n = 5$ , data not shown), indicating that release is mediated by Ca<sub>v</sub>2.1 and Ca<sub>v</sub>2.2 channels at this synapse. To determine whether D1R and GABA<sub>B</sub>R selectively regulate one of these channel types, we applied Ca<sub>v</sub>2.1- and Ca<sub>v</sub>2.2-specific antagonists ω-agatoxin-TK (AgaTx, 150 nM) or ω-conotoxin-GVIA (CTx, 3 μM; Bender and Trussell, 2009), followed by either SKF or baclofen. Though both AgaTx and CTx suppressed Ca transients, neither occluded modulatory effects of D1R or GABA<sub>B</sub>R. (Figures 4E and 4F; Norm ΔF/F =  $0.75 \pm 0.06$  and  $0.47 \pm 0.06$  for AgaTx and AgaTx+SKF, respectively,  $n = 7$ ,  $p < 0.05$ ; Norm ΔF/F =  $0.64 \pm 0.08$  and  $0.44 \pm 0.08$  for AgaTx and AgaTx+Bac, respectively,  $n = 6$ ,  $p < 0.05$ ; Norm ΔF/F =  $0.82 \pm 0.04$  and  $0.57 \pm 0.06$  for CTx and CTx+SKF, respectively,  $n = 6$ ,  $p < 0.05$ ; Norm ΔF/F =  $0.80 \pm 0.06$  and  $0.48 \pm 0.07$  for CTx and CTx+Bac, respectively,  $n = 7$ ,  $p < 0.05$ ; signed-rank test for all comparisons). Thus, these data indicate that D1Rs and GABA<sub>B</sub>Rs both suppress excitatory transmission through Ca<sub>v</sub>2.1 and Ca<sub>v</sub>2.2 channels, although they act via different signaling cascades.

Given that D1R suppression can occur in conjunction with GABA<sub>B</sub>R suppression within the same bouton, it is possible that they regulate different biophysical properties of presynaptic CaVs. We reasoned that differential CaV modulation could account for differences in how D1Rs and GABA<sub>B</sub>Rs regulate vesicle release. Interestingly, a similar dissociation between regulation of  $P_R$  and short-term dynamics has been observed

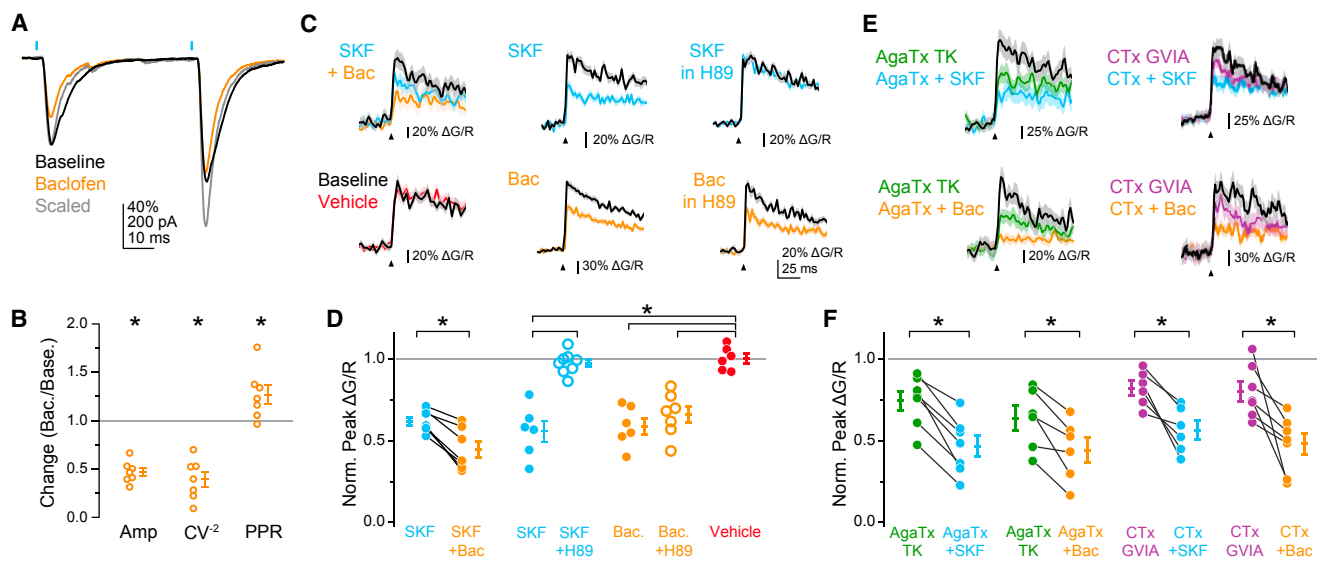


**Figure 4. GABA<sub>B</sub>R Suppresses Presynaptic Calcium Influx with Canonical Increase in PPR**

- (A) Example of GABA<sub>B</sub>R modulation of cPFC oEPSCs and PPR (as in Figure 2A).
- (B) Summary of GABA<sub>B</sub>R modulation of oEPSC amplitude, CV<sup>-2</sup>, and PPR.
- (C) Examples of AP-evoked bouton calcium transients for D1R followed by GABA<sub>B</sub>R activation, D1R activation alone, D1R activation with 10 μM H89, vehicle application, GABA<sub>B</sub>R activation alone, or GABA<sub>B</sub>R activation with H89. Data are plotted as mean ΔG/R with shaded error bars indicating within-condition SEM.
- (D) Summary of change in peak ΔG/R for conditions in (C).
- (E) Example responses, as in (C), for effects of D1R or GABABR activation with concurrent Cav2.1 or Cav2.2 block.
- (F) Summary of change in peak ΔG/R for conditions in (E).

at hippocampal Schaffer collateral synapses. At this synapse, it has been proposed that vesicle release is mediated by a small number of CaVs (i.e., nanodomain release configuration, Scimemi and Diamond, 2012). In such a configuration, reductions in the amount of Ca fluxed by single CaVs during an AP ( $i_{\text{CaV}}$ ) can suppress Ca influx, reduce initial  $P_R$ , and increase PPR through an accumulation of Ca bound to vesicular release machinery (Jackman and Regehr, 2017; Zucker and Regehr, 2002). By contrast, reductions in the probability a CaV opens in response to an AP ( $p_{\text{open}}$ ) could have multiple effects. If many CaVs contribute to vesicle release (i.e., microdomain release configuration), then a reduction in  $p_{\text{open}}$  should simply reduce the total Ca current ( $I_{\text{CaV}}$ ) and have effects on  $P_R$  and PPR similar to reductions in Ca current per channel (e.g., single-channel current,  $i_{\text{CaV}}$ ). However, if very few CaVs contribute to vesicle release, then the likelihood of local Ca influx failures on individual trials ( $I_{\text{CaV}} = 0$ ) becomes non-negligible, and on these trials a reduction in  $P_R$  may be followed by a lack of facilitation due to the absence of Ca accumulation at Ca sensors that mediate release.

Due to differences in dissociation rate, the divalent channel antagonists manganese (Mn) and cadmium (Cd) can differentially suppress  $i_{\text{CaV}}$  or  $p_{\text{open}}$ , respectively. Mn, which can bind and dissociate from a CaV many times within the time course of an AP, functionally reduces  $i_{\text{CaV}}$ , similar to lowering extracellular Ca. In contrast, Cd dissociation rates are an order of magnitude slower than an AP (0.02 ms<sup>-1</sup>; Thévenod and Jones, 1992). At subsaturating concentrations, individual CaVs will likely be completely blocked or not blocked by Cd during the time course

of a single AP. As such, Cd reduces  $p_{\text{open}}$ . At Schaffer collateral synapses, Mn and Cd both reduced EPSC amplitude, but PPR increased only with Mn (Scimemi and Diamond, 2012), suggesting that these synapses operate in the nanodomain configuration. To test whether long-range inputs into PFC also show different responses to reductions in  $i_{\text{CaV}}$  or  $p_{\text{open}}$ , we suppressed CaVs using Mn or Cd at cPFC inputs (Figure 5). As with Schaffer collaterals, we observed a dose-dependent effect of Mn on both reducing oEPSC amplitude and increasing PPR (Figures 5A and 5B; n = 8; [Mn<sup>2+</sup>] = 50, 100, and 200 μM; Norm Amp. = 0.87 ± 0.03, 0.71 ± 0.05, and 0.47 ± 0.05; Norm PPR = 1.09 ± 0.03, 1.13 ± 0.06, and 1.28 ± 0.07). By contrast, we observed a dose-dependent effect of Cd on decreasing oEPSC amplitude, but no corresponding increase in PPR (Figures 5C and 5D; n = 7; [Cd<sup>2+</sup>] = 2, 5, 7.5, and 10 μM; Norm Amp. = 0.94 ± 0.03, 0.69 ± 0.04, 0.41 ± 0.03, and 0.30 ± 0.03; Norm PPR = 0.98 ± 0.04, 0.94 ± 0.06, 0.94 ± 0.06, and 0.88 ± 0.07). The relationship between PPR and oEPSC amplitude was remarkably similar for Mn and GABA<sub>B</sub>R activation and for Cd and D1R activation (Figure 5E). Further, both Mn and Cd reduced CV<sup>-2</sup>, consistent with D1R and GABA<sub>B</sub>R activation (Figure 5F; Mn Norm CV<sup>-2</sup> = 0.70 ± 0.16, 0.53 ± 0.19, and 0.41 ± 0.14; Cd Norm CV<sup>-2</sup> = 0.84 ± 0.19, 0.58 ± 0.09, 0.42 ± 0.15, and 0.33 ± 0.12).

#### Differential Modulation of CaVs by D1Rs and GABA<sub>B</sub>Rs Account for Differences in STP

Based on these results, we hypothesized that D1Rs and GABA<sub>B</sub>Rs could have distinct effects on short-term facilitation if D1Rs mimics Cd and GABA<sub>B</sub>Rs mimics Mn. This could

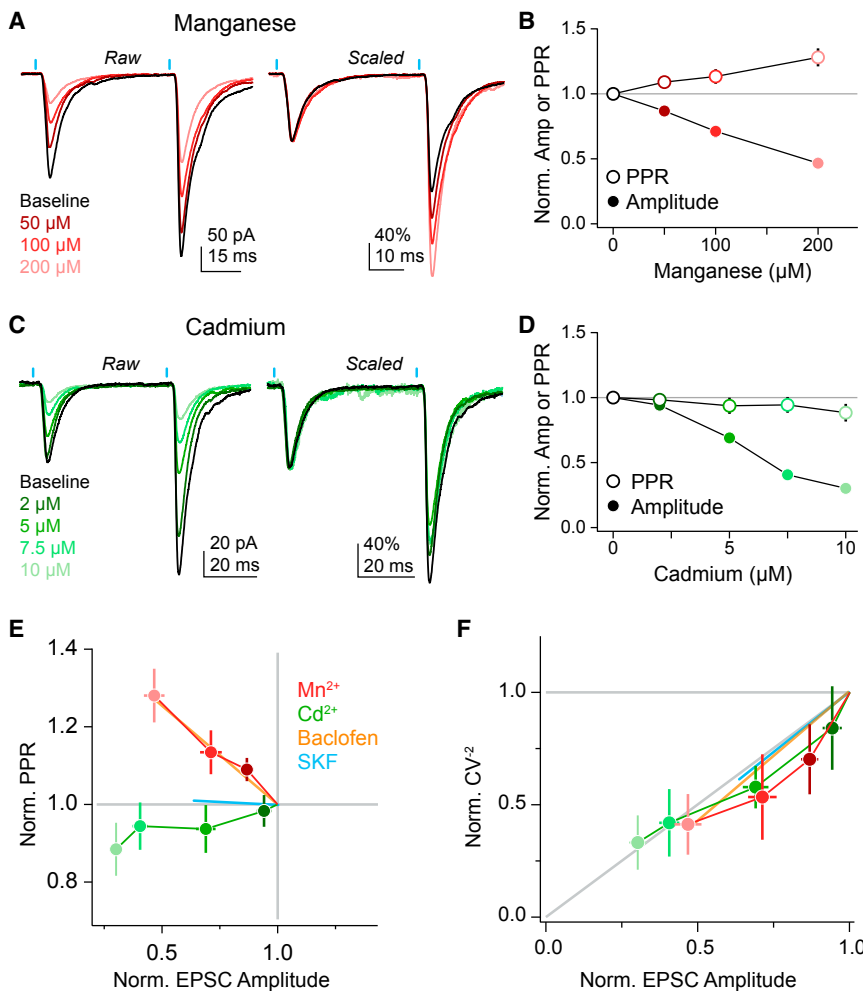


**Figure 5. CaV Antagonists with Different Binding Kinetics Mimic D1R and GABA<sub>B</sub>R**

(A) Example cell with increasing manganese concentrations. Left, raw oEPSCs; right: scaled to initial oEPSC amplitude.

(B) Summary for manganese effects on oEPSC amplitude and PPR.

(C) Same as (A) and (B), but for cadmium.

(E and F) Normalized PPR and CV<sup>-2</sup> for manganese and cadmium conditions versus normalized oEPSC amplitude. D1R and GABA<sub>B</sub>R modulation are shown in cyan and orange, respectively, for reference.

(Figure 6C). The variance predicted by dark noise and shot noise alone was subtracted from the measured variance to obtain variance related to CaV activity (Figure 6D).

Analysis of the resulting Ca transients is mathematically similar to EPSC nonstationary fluctuation analysis, but applied to imaging data instead of electrophysiological data (Quastel, 1997; Sigworth, 1980; Sabatini and Svoboda, 2000). Ca influx in a bouton can be modeled as a binomial process arising from  $N$  CaVs, each with single-channel current  $i$  and open probability  $p$ , and quantitative predictions can be made for how trial-to-trial variability is affected given changes to  $N$ ,  $i$ , or  $p$ . Within this framework, the mean-normalized variance should not change when reducing the single-channel current  $i$ , but it should increase with reductions in  $N$  and  $p$ . Importantly, the variance should

increase more for reductions in  $p$  than for similar reductions in  $N$ , especially in boutons where CaV open probability per AP is high (Figure S6C; Yasuda et al., 2003). Lastly, because we used propagating APs as our stimulus,  $i$  and  $p$  reflect the single-channel Ca charge transfer and overall channel open probability per AP, respectively.

In time-locked control conditions, AP-evoked bouton Ca transients were stable for > 100 trials (Figure 6E). All subsequent pharmacological experiments were therefore limited to a maximum of 100 trials. Baseline and post-drug measurements of 40–50 trials were separated by ~10 min to allow for drug equilibration. Both D1R and GABA<sub>B</sub>R activation suppressed presynaptic Ca influx (Figures 6F and 6G), but decreases in  $CV_{CaV}^{-2}$  were observed primarily with D1R, not GABA<sub>B</sub>R, activation (Figures 6H–6K; for D1R and GABA<sub>B</sub>R, respectively:  $n = 6$  and 6; Norm  $CV_{CaV}^{-2} = 0.18 \pm 0.07$  and  $0.94 \pm 0.05$ ; Norm Peak  $\Delta G/R = 0.56 \pm 0.06$  and  $0.59 \pm 0.05$ ; chi-square statistic = 23.88,  $p < 0.001$ , Kruskal-Wallis; SKF versus baclofen  $p < 0.001$ ; rank-sum test with Holm-Sidak correction). Like GABA<sub>B</sub>Rs, reducing extracellular Ca suppressed Ca signals with little change in  $CV_{CaV}^{-2}$  (Figure 6L;  $n = 6$ ;  $\Delta CV_{CaV}^{-2} = 0.95 \pm 0.05$ ; Norm  $\Delta F = 0.39 \pm 0.05$ ;  $\Delta Ca^{2+}$  versus baclofen  $p = 0.92$ ; rank-sum

occur through several biophysical mechanisms. For example, GABA<sub>B</sub>R-induced changes in channel gating, perhaps by depolarizing the voltage dependence of activation or increasing the reluctance of channel opening, could reduce the channel open duration during an AP (Huynh et al., 2015; Mintz and Bean, 1993; Patil et al., 1996). This would be functionally equivalent to Mn application, as it would produce a partial suppression of Ca influx per channel. By contrast, D1R-dependent modulation that reduces the likelihood that a CaV opens at all in response to an AP would mimic Cd, as it would produce all-or-none suppression of Ca influx per channel.

To test the hypothesis that D1Rs and GABA<sub>B</sub>Rs differentially regulate the way CaVs respond to AP stimuli, we applied optical fluctuation analysis (OFA) to PFC bouton Ca signals (Carter and Jahr, 2016; Sabatini and Svoboda, 2000). We made whole-cell recordings and visualized AP-evoked Ca signals in axonal boutons (Figures 6A and 6B). Boutons were always imaged in serial pairs to ensure that trial-to-trial variability was uncorrelated and thus unlikely to be the result of AP conduction failures (Figures S6A and S6B). Both the mean amplitude,  $\Delta F$ , and variance,  $\sigma_F^2$ , were measured immediately following the AP to limit signal contamination from sources other than the bouton CaVs

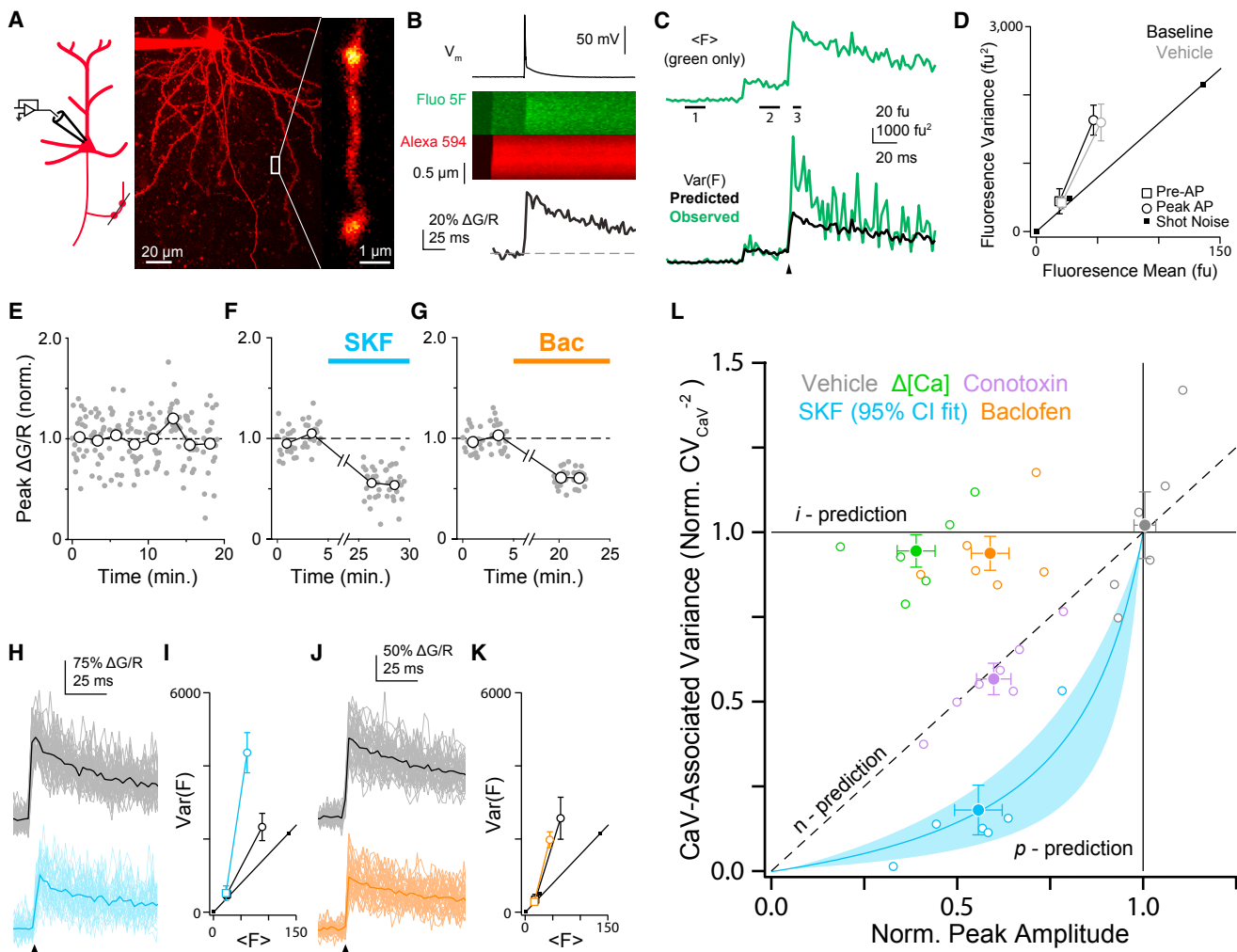


**Figure 6. D1R and GABA<sub>B</sub>R Modulate Different Biophysical Properties of Presynaptic CaVs**

(A) OFA recording configuration. Left: Schematic for local axonal bouton imaging. Center: Z-projection image of dendritic and axonal processes containing Alexa 594. Right: magnification of center panel highlighting two boutons in series along axon branch.

(B) Bouton calcium response. Top: Mean membrane voltage ( $V_m$ ) in response to short-duration somatic current injection (2–2.5 nA × 2 ms). Middle: Example mean fluorescence response of axonal bouton over 20 trials (note: two-photon excitation begins with 50 ms delay to measure dark noise). Bottom: Mean  $\Delta G/R$  response as a function of time for data in middle panel (dashed line indicates baseline fluorescence; time points before laser excitation excluded for clarity).

(C) Top: mean response, green channel only. Numbers and black bars indicate time range for calculating (1) dark noise, (2) baseline, and (3) peak mean and variance. Bottom: variance,  $Var(F)$ , compared to variance predicted by dark and shot noise alone (black trace). Arrowhead: AP timing.

(D) Variance-Mean plot before and after vehicle application. Variance and mean fluorescence were measured at baseline (empty squares, “Pre-AP”) and peak response (empty circles, “Peak AP”) time ranges (ranges 2 and 3 from Figure 6C, respectively). All values corrected for dark noise. Shot noise measurements shown for reference (filled squares and linear fit). Error bars are 1 SD from estimates obtained from multiple time points per range.

(E) Peak  $\Delta G/R$  response of a single bouton over time. Gray points represent individual trials, open circles are average of 20 trials.

(F and G) Peak  $\Delta G/R$  responses of boutons before and after D1R or GABA<sub>B</sub>R activation.

(H) Mean  $\Delta G/R$  with individual trials for baseline (top) and post-drug (bottom) conditions with D1R activation.

(I) Variance-mean plot for one cell before (black) and after (cyan) D1R activation (same cell as in H).

(J and K) Example cell with GABA<sub>B</sub>R activation, as in (H) and (I).

(L) Normalized CaV-associated Variance versus Normalized Peak Amplitude. Vehicle, peak  $\Delta G/R = 1.01 \pm 0.03$ ,  $CV_{CaV}^{-2} = 1.02 \pm 0.10$ ,  $n = 6$ .

test with Holm-Sidak correction). Thus, these data indicate that GABA<sub>B</sub>Rs limit Ca influx from individual CaVs per AP, whereas D1Rs decrease the average number of CaVs that open in response to an AP, which could be due to a change in  $N$  or  $p$ .

To determine whether D1Rs reduce CaV number or open probability, we compared D1R effects to application of a subsa-

turating dose of  $\omega$ -conotoxin MVIIIC (35 nM). Because the dissociation rate of  $\omega$ -conotoxin MVIIIC is substantially slower than the time course of these experiments (McDonough et al., 1996), it should act as an irreversible CaV antagonist and effectively reduce  $N$ . Indeed,  $CV_{CaV}^{-2}$  decreased linearly with Ca response amplitude after conotoxin application (Figure 6L;  $n = 7$ ; Norm

$CV_{CaV}^{-2} = 0.57 \pm 0.05$ ; Norm  $\langle \Delta F \rangle = 0.60 \pm 0.05$ ). This contrasts with D1R results where  $CV_{CaV}^{-2}$  reduced more quickly than  $\langle \Delta F \rangle$  (conotoxin versus SKF  $p < 0.001$ ; rank-sum test with Holm-Sidak correction), suggesting that D1Rs do not reduce the number of channels at the bouton.

Because D1Rs suppressed  $CV_{CaV}^{-2}$  more strongly than predicted by reductions in  $N$ , we next asked whether D1R suppression was consistent with a reduction in  $p$ . In cases where  $p$  is modulated, the steepness of the change in  $CV_{CaV}^{-2}$  depends strongly on the baseline open probability; thus, one can fit observed changes in  $CV_{CaV}^{-2}$  and  $\langle \Delta F \rangle$  to a nonlinear function parameterized by different estimates of baseline CaV open probability (Figure S6C). The observed changes in  $CV_{CaV}^{-2}$  and  $\langle \Delta F \rangle$  after D1R activation agreed well with a baseline open probability of 0.83 (95% confidence interval = 0.73–0.93), consistent with more direct measures of  $p$  at other terminals (Borst and Sakmann, 1998; Li et al., 2007). Taken together, these data indicate that D1Rs and GABA<sub>B</sub>Rs suppress presynaptic CaV  $p_{open}$  and  $i_{CaV}$ , respectively (Figure 6L).

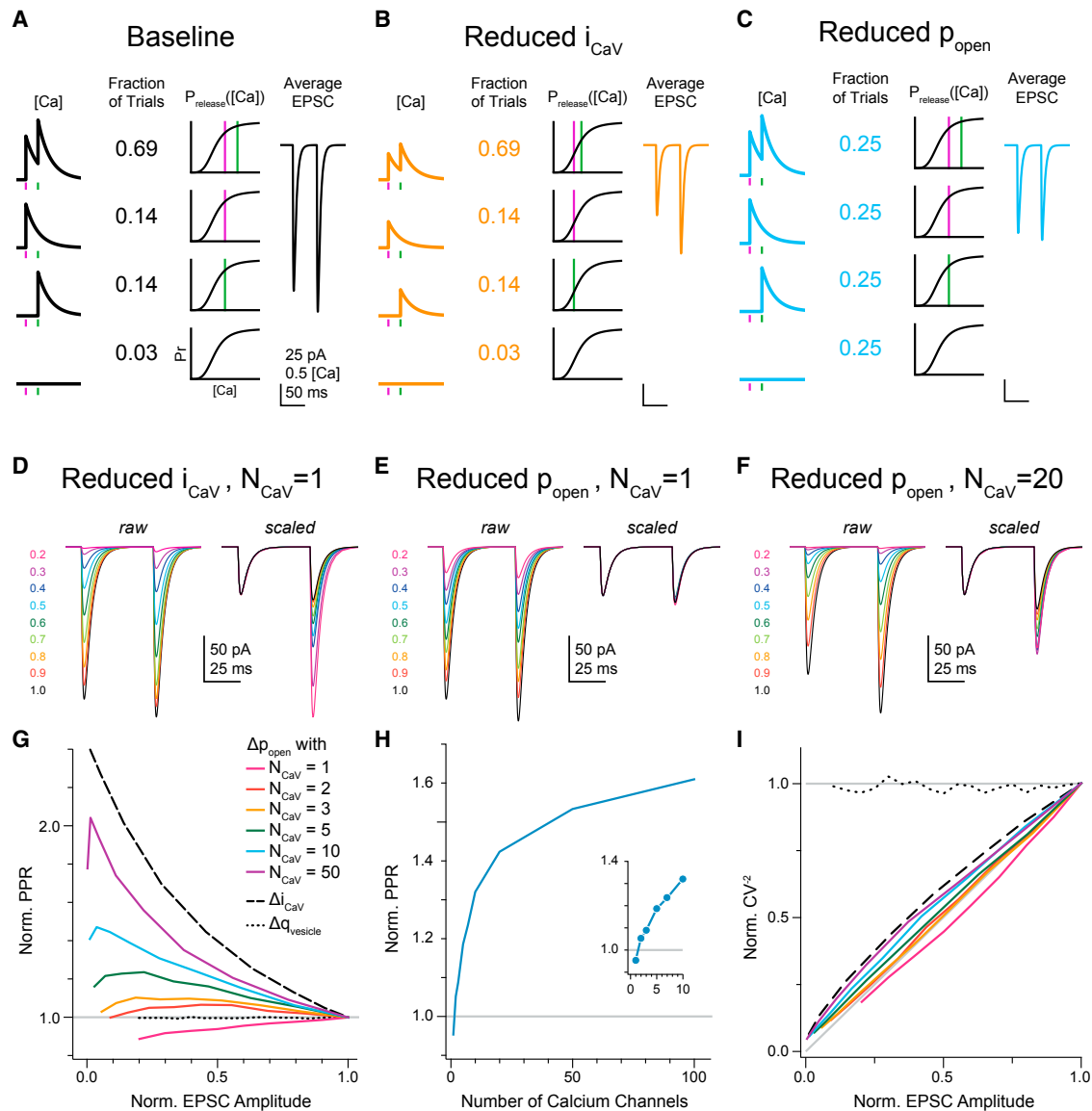
To determine whether the different biophysical mechanisms of CaV modulation predicted by OFA are sufficient to explain the differing effects of D1Rs and GABA<sub>B</sub>Rs on STP, we developed a reduced synaptic model (Figure 7A; Table S1). We simulated 50 synapses onto a single postsynaptic neuron, where each presynaptic terminal contained a constant number of CaVs. Channel activity was simulated as a simple binomial process to adapt OFA data directly into the model, and vesicle  $P_R$  was calculated as a Hill function of the Ca concentration per bouton (Stanley, 2016; Zucker and Regehr, 2002). Note that the resulting total number of vesicles was convolved with an AMPA-like sum of exponential waveforms for visualization, but analysis of EPSC amplitude and PPR was based solely on mean quantal content (see STAR Methods).

We began by assuming that vesicle release was driven by only one CaV per synapse with an open probability of 0.83 per AP (derived from OFA analysis, Figure 6L; Bucurenciu et al., 2008; Scimemi and Diamond, 2012; Stanley, 2016). Given this open probability, four different Ca transients were observed with differing probabilities in response to paired-pulse stimulation (Figure 7A, four rows). In most cases, both APs resulted in a CaV opening (69% of trials), but in some cases the CaV opened in response to only the first or second AP (14% each) or to neither (3%). This is a direct result of the CaV openings being independent across channels and trials. These probabilities, when translated into release via the Hill function ( $S = 0.25$ , cooperativity = 3.72; Scimemi and Diamond, 2012) and aggregated across all 50 simulated synapses, resulted in modest paired-pulse facilitation of quantal content (model PPR = 1.14, compared to measured oEPSC PPR of  $1.31 \pm 0.09$ ,  $1.31 \pm 0.08$ , and  $1.10 \pm 0.08$  for iPFC, cPFC, and vHPC, respectively).

Given these baseline conditions, we next altered either the CaV single-channel current ( $i$ ) or open probability ( $p$ ) per AP to an extent that matched the D1R and GABA<sub>B</sub>R OFA data (0.6 of baseline for either model parameter, Figures 7B and 7C; compared to peak ΔG/R amplitude reduction to  $0.56 \pm 0.06$  and  $0.59 \pm 0.05$  of baseline for D1R and GABA<sub>B</sub>R, Figure 6L). Modulation of  $i$  strongly reduced  $P_R$  due to the Hill function nonlinearity described above. As such, differences in residual

Ca levels after the first AP nonlinearly enhanced  $P_R$  on the second AP, and PPR was increased. By contrast, when only one CaV contributed to release per synapse, modulation of  $p$  did not change Ca transient amplitude ratios or residual Ca; instead, modulation of  $p$  decreased the likelihood of two APs both eliciting successful Ca influx and increased the likelihood that Ca influx would occur on only the first AP, only the second AP, or not at all. Thus, when aggregated across all synapses and trials, the net EPSC amplitude was reduced without increasing PPR. In fact, more dramatic reductions in  $p$  led to a small decrease in PPR. This is because our simulations were tuned to evoke modest PPF at baseline, matching empirical observations (Figure 2), and as  $p$  decreased, the likelihood of successful Ca influx for both APs (and thus, facilitation) approached zero. As a result, the net EPSC will be weighted more heavily toward Ca influx failures, and PPR will trend toward 1, which would appear as a decrease when normalized to facilitation at baseline (Figures 5C–5E). This result did not depend on the exact values chosen for the Ca concentration decay time constant or interval between APs and was also observed when synapses had a distribution of channel numbers and Ca decay time constants (Figures S7A–S7C).

Synaptic facilitation can occur through multiple mechanisms, including slow clearance of Ca from the presynaptic terminal (i.e., the residual Ca hypothesis, Jackman and Regehr, 2017), saturation of endogenous Ca buffers (i.e., the buffer hypothesis, Blatow et al., 2003; Rozov et al., 2001), or interactions with a high-affinity Ca sensor that has Ca dissociation kinetics that are slower than the paired-pulse interval (e.g., synaptotagmin7, bound Ca hypothesis, Jackman et al., 2016). While the simulations described above use residual Ca as a mechanism for facilitation in a highly reduced manner, similar results were obtained with a model that incorporates three additional, more realistic features (Figures S7D–S7I). First, rather than simulating the bouton as a point, the linearized buffer approximation (“LBA,” Naraghi and Neher, 1997; Neher, 1998) was used to approximate Ca concentration as a function of distance from the CaV. Then, Ca-dependent short-term facilitation was generated by scaling  $P_R$  by a second, higher-affinity Hill function with Ca affinity and cooperativity derived from synaptotagmin7 (see STAR Methods and Table S1). Last, a simple model of vesicle depletion and replenishment was added, which is critical to generate Ca-dependent short-term facilitation in this form of model (Scimemi and Diamond, 2012). Paralleling results from our simpler model, the same basic pattern of canonical and noncanonical modulation with changes in  $i$  and  $p$  was observed when only a few CaVs were responsible for release, especially for CaV-vesicle distances that reflect tight diffusional coupling (< 25 nm, Bucurenciu et al., 2010; Nakamura et al., 2018; Scimemi and Diamond, 2012; Figure S7D–S7H). This is likely because noncanonical STP due to suppression of  $p$  occurs upstream of release machinery and Ca diffusion dynamics, and because the “paired-pulse facilitation” of intracellular Ca also trends toward 1 in these conditions. To further illustrate this point, we built a linear phenomenological model of short-term facilitation (Figures S7J–S7L; Betz, 1970; Varela et al., 1997; Markram et al., 1998). This model makes no assumptions about the cellular mechanisms that support facilitation; its only requirement is that facilitation is Ca

**Figure 7. Model of Synapse Reproduces Non-Canonical Presynaptic Modulation**

(A) Reduced model of presynaptic release. Rows are possible trial outcomes for different CaV  $p_{open}$  values for a single bouton given release mediated by one presynaptic CaV. Columns, from left to right: presynaptic calcium concentration (purple/green tick marks indicate first and second AP), fraction of trials where this occurred,  $P_R$  as a function of calcium concentration (calcium concentrations for two APs indicated by purple/green lines), total average EPSC across synapses and trials.

(B and C) As in (A), but with CaV single-channel current  $i_{CaV}$  or open probability  $p_{open}$  reduced to 60% of baseline to mimic OFA results for GABA<sub>B</sub>R and D1R, respectively.

(D) Suppression of EPSC by graded reduction in  $i_{CaV}$  with release mediated by one presynaptic CaV. Left: Colors indicate fraction reduction in  $i_{CaV}$ . Right: scaled to first EPSC amplitude.

(E) Suppression of EPSC by graded reduction in  $p_{open}$ , as in (D).

(F) Suppression of EPSC by graded reduction in  $p_{open}$ , with release mediated by 20 CaVs.

(G) Normalized PPR versus normalized EPSC amplitude for reductions in  $i_{CaV}$ ,  $q_{vesicle}$  or  $p_{open}$  under different numbers of presynaptic CaVs mediating release.

(H) Normalized PPR with reduction in  $p_{open}$  to 60% of baseline, as a function of number of presynaptic CaVs mediating release. Grey line indicates no change in PPR. Inset: Expanded view of first few channel numbers.

(I) Normalized  $CV^{-2}$  plotted against normalized EPSC amplitude for reductions in  $i_{CaV}$ ,  $q_{vesicle}$ , or  $p_{open}$  under different numbers of presynaptic CaVs mediating release.

dependent. Even here, we observed the same differences in PPR modulation by changes in  $i$  and  $p$ . Thus, these models can account for different mechanisms by which facilitation could occur, including buffer saturation or a high-affinity Ca sensor with slow kinetics, provided that facilitation depends on residual Ca in some way.

This PPR dependence on  $i$  but not  $p$  was consistent across a range of parameter reductions (Figures 7D and 7E). As expected, reductions in quantal size  $q_{\text{vesicle}}$  did not alter PPR, and the insensitivity of PPR to reductions in  $p$  was diminished as the number of CaVs driving release per synapse increased (Figures 7F–7H). PPR invariance was observed only when few channels (1–3), either uniformly or randomly distributed across boutons, contributed to release (Figures 7D, 7F–7H, S7C, S7F, S7I, and S7L). Importantly, this model also reproduced our finding that CV analysis indicated a presynaptic site of action for all tested presynaptic configurations but not the postsynaptic modulation of  $q_{\text{vesicle}}$  (Figure 7I). Taken together with OFA results, these data indicate that the different effects of D1Rs and GABA<sub>B</sub>Rs on short-term facilitation can, in principle, be explained by differential modulation of presynaptic CaVs.

### Non-canonical Presynaptic Modulation Strongly Suppresses Ongoing Activity

Given these differences in STP, we next sought to determine how ongoing activity was shaped by these two neuromodulators. We stimulated cPFC inputs expressing ChR2 with trains of 10 light pulses at either a regular frequency of 20, 10, or 5 Hz or at a combination of these three frequencies (Figures 8A–8F). We found that stimulation of D1Rs consistently suppressed the entire sequence of all ten oEPSCs (Figure 8A) and often suppressed oEPSCs that occurred at the end of the train to the greatest extent (Figures 8B and 8E). But due to increased PPR, GABA<sub>B</sub>R suppression of oEPSCs was clearer at the beginning of trains, with little difference in oEPSC amplitude toward the end (Figures 8C–8E). This pattern was observed across multiple frequencies as well as with stimulation of variable intervals (Figure S8A). We quantified the “charge ratio,”  $\Delta R_Q$ , which measures the suppression of trains of oEPSCs normalized to the suppression of the first oEPSC. When  $\Delta R_Q < 1$  or  $\Delta R_Q > 1$ , the entire sequence of stimuli was suppressed more or less than the initial stimulus, respectively. D1Rs and GABA<sub>B</sub>Rs showed significantly different values of  $\Delta R_Q$  across multiple frequencies (Figure 8F,  $\Delta R_Q$ : SKF,  $n = 7$ , 20 Hz =  $0.73 \pm 0.08$ , 10 Hz =  $0.71 \pm 0.05$ , 5 Hz =  $0.70 \pm 0.08$ , Mixed Intervals =  $0.71 \pm 0.05$ ;  $\Delta R_Q$ : baclofen,  $n = 7$ , 20 Hz =  $1.38 \pm 0.06$ , 10 Hz =  $1.33 \pm 0.12$ , 5 Hz =  $1.14 \pm 0.08$ , Mixed Intervals =  $1.34 \pm 0.08$ ; chi-square statistic = 40.48,  $p < 0.001$ , Kruskal-Wallis; SKF versus baclofen, 20 Hz  $p < 0.001$ , 10 Hz  $p < 0.001$ , 5 Hz  $p = 0.002$ , Mixed Intervals  $p < 0.001$ ; rank-sum test with Holm-Sidak correction). These data suggest that GABA<sub>B</sub>Rs act as a high-pass filter on synaptic transmission, whereas D1Rs act to suppress synaptic transmission independent of event timing.

We next sought to test whether these differences in STP translate to differences in AP generation in more realistic, *in vivo*-like conditions. We performed current-clamp experiments where

we injected a noisy current waveform stimulus that was comprised of randomly generated simulated EPSCs and IPSCs in order to depolarize the postsynaptic cell and generate APs. We also generated a train of LED pulses with shuffled intervals, ranging from 1 to 20 Hz in frequency, to activate long-range ChR2-expressing cPFC inputs (Figure 8G). Stimulation of these inputs by the LED generated short-latency APs in the recorded postsynaptic neuron (Figures 8H–8I). Importantly, due in part to the injected noisy current waveform, LED stimulation did not generate APs on every trial. This allowed us to apply D1R or GABA<sub>B</sub>R agonists and test whether these neuromodulators suppress ChR2-mediated spiking in different ways depending on ChR2 stimulation frequency. At the slowest frequency of 1 Hz, LED-evoked spiking was suppressed significantly by both D1R and GABA<sub>B</sub>R agonists (norm spike frequency within 12 ms of LED =  $0.43 \pm 0.07$  and  $0.38 \pm 0.05$  for SKF and baclofen, respectively). However, as the input LED frequency increased, GABA<sub>B</sub>R-mediated suppression weakened significantly, whereas D1R-mediated suppression remained similar across all frequencies (Figures 8I, 8J, and S8B; Norm frequency after SKF =  $0.43 \pm 0.07$ ,  $0.55 \pm 0.07$ ,  $0.49 \pm 0.09$ , and  $0.50 \pm 0.20$  for 1, 5, 10, and 20 Hz, respectively,  $n = 6$ , chi-square statistic = 1.25,  $p = 0.74$ , Kruskal-Wallis; Norm frequency after baclofen =  $0.38 \pm 0.05$ ,  $0.82 \pm 0.06$ ,  $0.74 \pm 0.06$ , and  $0.82 \pm 0.04$  for 1, 5, 10, and 20 Hz, respectively,  $n = 8$ , chi-square statistic = 16.08,  $p < 0.05$ , Kruskal-Wallis;  $p < 0.05$  for baclofen 1 Hz versus all other frequencies; rank-sum test with Holm-Sidak correction). Thus, these data indicate that GABA and dopamine have differential effects on synaptic integration, with GABA facilitating the transmission of inputs that occur in high-frequency bursts and dopamine suppressing transmission in a frequency-independent manner.

### DISCUSSION

We demonstrate here that activation of the D1 dopamine receptor suppresses a subset of excitatory long-range and local inputs in PFC. By reducing presynaptic CaV open probability, D1R can suppress vesicle  $P_R$  without a parallel increase in short-term facilitation. This non-canonical presynaptic neuromodulation suppresses AP generation across multiple stimulation frequencies and is well explained by a simple synapse model where vesicle release is mediated by a small number of CaVs.

These results provide mechanistic insight into how modulation of specific biophysical properties of presynaptic CaVs can result in surprisingly large differences in synaptic transmission and STP. These data address a long-standing puzzle related to prefrontal dopaminergic modulation by explaining how a neuromodulator can have little effect on paired-pulse facilitation despite a presynaptic site of action (Gao et al., 2001; Seamans et al., 2001; Gao and Goldman-Rakic, 2002; Seamans and Yang, 2004). In addition to prefrontal cortical synapses, the mechanisms identified here may account for similar observations made in a diverse set of synapses and neuromodulatory systems (Behr et al., 2000; Delaney et al., 2007; Holmes et al., 2017; Li et al., 2012; Tejeda et al., 2017). In future work, it will be critical to understand the role that distinct canonical and non-canonical presynaptic modulatory pathways play in information transfer in neuronal networks.

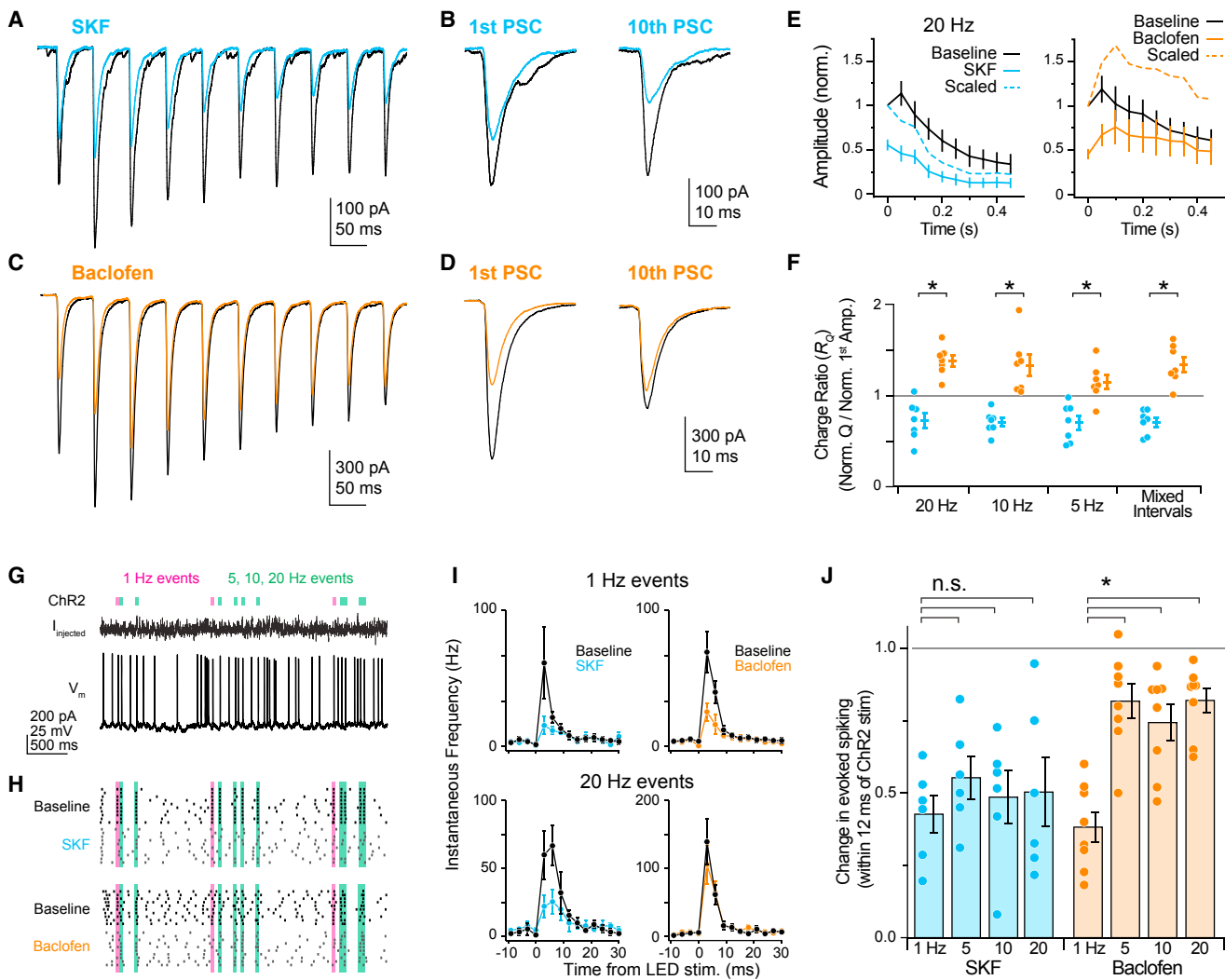


**Figure 8. D1R and GABA<sub>B</sub>R Differentially Filter Ongoing Synaptic Activity**

(A) Train of ten oEPSCs at 20 Hz before and after D1R stimulation.  
 (B) Expanded view of first and tenth oEPSC.  
 (C) and (D) As in (A) and (B) but with GABA<sub>B</sub>R stimulation.  
 (E) Modulation of ongoing activity at 20 Hz. Left: oEPSC amplitudes before and after D1R stimulation. Right: As on left, but with GABA<sub>B</sub>R activation.  
 (F) Suppression of ongoing activity relative to first amplitude. The charge ratio was consistently larger for GABA<sub>B</sub>R activation than for D1R activation across multiple frequencies. “Mixed Intervals” was a predetermined combination of three inter-stimulus intervals at 5, 10, and 20 Hz, shuffled.  
 (G) Recording configuration for current-clamp experiments. Top: Train of LED pulses to activate ChR2-positive long-range inputs from cPFC (color-coded by preceding interval being equal to or faster than 1 Hz for pink and green tic marks, respectively). Middle: Simulated PSC waveform injected into the soma through the recording electrode. Bottom: Recorded membrane voltage.  
 (H) Modulation of spike timing. Top: Example raster plot (same cell as in G) of spike times over trials with different injected PSC waveforms before (above, “Baseline”) and after (below, “SKF”) D1R activation. Bottom: As above, but with GABA<sub>B</sub>R activation. Black tic marks indicate timing of 1 Hz and > 1 Hz LED pulses, respectively.  
 (I) Modulation of LED-evoked spiking. Top: Instantaneous frequency of spiking aligned to 1Hz LED stimuli, averaged across cells, before and after D1R and GABA<sub>B</sub>R activation for left and right plots, respectively ( $n = 6$  and 8 for D1R and GABA<sub>B</sub>R). Bottom: As above, but aligned to 20 Hz LED stimuli.  
 (J) Summary data of neuromodulation of LED-evoked spiking. Bars are mean  $\pm$  SEM. Circles are single cells.

### CaV-Vesicle Coupling and Presynaptic Neuromodulation

The facilitation-independent form of presynaptic modulation described here requires that release is mediated by nanodomain coupling between only a few CaVs per vesicle (Figure 7; Scimemi and Diamond, 2012). This configuration is similar to other synapses,

including the mature calyx of Held (Fedchyshyn and Wang, 2005), cochlear and retinal ribbon synapses (Goutman and Glowitzki, 2007; Jarsky et al., 2016), hippocampal basket cell boutons (Bucurenciu et al., 2010), and Schaffer collaterals (Scimemi and Diamond, 2012). In the nanodomain configuration, the overall Ca concentration that triggers release is strongly influenced

by the stochastic opening of individual CaVs, and as such, slow CaV antagonists like Cd suppress release without increasing PPR (Figure 5; Hefft et al., 2002; Hjelmstad, 2004; Scimemi and Diamond, 2012). By contrast, when release is mediated by Ca microdomains, the overall Ca concentration is less influenced by single-channel stochasticity. At microdomain synapses, including the immature calyx of Held (Fedchyshyn and Wang, 2005), Cd suppresses release while also increasing PPR (Otis and Trussell, 1996). We explored this difference between nanodomains and microdomains in our reduced model by examining how changing the number of functional CaVs per synapse affects the response of the model synapse to modulation of  $i_{CaV}$  or  $p_{open}$  (Figure 7). Indeed, we observed that reductions in CaV  $p_{open}$  preserved paired-pulse facilitation in the nanodomain-like configuration, but increased facilitation in the microdomain-like configuration. These differences have been proposed previously (Eggermann et al., 2011) and may account for why D1Rs suppress release with and without changes in PPR at different synapses (e.g., Wang et al., 2012).

Presynaptic gain modulation has been observed with several synapses and neuromodulators. At hippocampal Schaffer collaterals, where release is driven by few CaVs, reducing CaV  $p_{open}$  with Cd does not increase PPR (Scimemi and Diamond, 2012). At the perforant pathway synapse in subiculum, D1R also suppresses presynaptic gain (Behr et al., 2000). In the nucleus accumbens, excitatory inputs from amygdala, but not ventral hippocampus, display PPR-independent  $P_R$  suppression (Tejeda et al., 2017). At this synapse, both kappa-opioid receptors (KORs) and GABA<sub>B</sub>R suppress  $P_R$ ; however, KORs do not change PPR, whereas GABA<sub>B</sub>Rs increase PPR. Presynaptic gain modulation at other synapses, including KOR suppression in the bed nucleus of the stria terminalis and noradrenergic suppression in central amygdala, has been attributed to a reduction in the number of presynaptic release sites (Delaney et al., 2007; Li et al., 2012; but see Saviane and Silver, 2006). Taken together, the prevalence of neuromodulators that suppress release without increasing PPR throughout the brain suggests that presynaptic gain modulation may be a more common phenomenon than previously appreciated.

### Possible Mechanisms of CaV Modulation

Both D1Rs and GABA<sub>B</sub>Rs are known to modulate HVA CaVs (Surmeier et al., 1995; Zhang et al., 2002; Kisilevsky et al., 2008; Chalifoux and Carter, 2011). Our imaging and pharmacological experiments suggest that GABA<sub>B</sub>Rs and D1Rs modulate AP-evoked Ca influx in a graded or all-or-none manner, respectively, at individual presynaptic CaVs. Multiple biophysical mechanisms could underlie these observations. GABA<sub>B</sub>Rs could modify AP waveform by recruiting inward rectifying potassium channels or modulating other potassium channels, though the former has not been observed in PFC pyramidal cell axons (Xia et al., 2014). Alternatively, partial reductions in the current fluxed by single CaVs per AP could result from a GABA<sub>B</sub>R-induced reduction in channel conductance, delayed time to first opening, or depolarized shift in voltage-dependent activation. The latter two possibilities seem most likely, as GABA<sub>B</sub>Rs have been shown to interact directly with CaVs via G<sub>βγ</sub> subunits to either induce a rightward shift in activation or

delay the time of first opening via the induction of a “reluctant state” (Huynh et al., 2015; Mintz and Bean, 1993; Patil et al., 1996), whereas GABA<sub>B</sub>R-mediated changes in channel conductance have not been reported. The PKA independence of CaV modulation by GABA<sub>B</sub>Rs observed in the current study suggests that a similar G<sub>βγ</sub> mechanism may be present at pre-frontal synapses.

D1R modulation was PKA dependent, similar to previous reports in basal ganglia (Surmeier et al., 1995; Zhang et al., 2002), and produced all-or-none reductions in AP-evoked CaV opening. This could be instantiated biophysically through alterations in gating modes, perhaps through modulation of beta subunits that increase channel opening latency to an extent that exceeds the duration of the AP (Luvisetto et al., 2004). Alternatively, hyperpolarized shifts in steady-state inactivation could reduce the number of channels available for activation by an AP. Such modulatory effects have been observed with D3 dopamine receptor-dependent regulation of Ca<sub>v</sub>3.2 channels at the axon initial segment (Bender et al., 2010; Yang et al., 2016; Clarkson et al., 2017). Ca<sub>v</sub>2 channels could be modified by similar mechanisms, especially during AP trains (Patil et al., 1998). Overall, these data suggest that further investigation into the signaling pathways and biophysics of CaV channel modulation by dopamine and other metabotropic receptors will yield greater insight into the diversity of synaptic neuromodulation in the axon.

### Functional Implications

Regulating synaptic gain is an important mechanism for shaping information transfer throughout the brain. Traditionally, gain modulation has been thought to occur at the postsynaptic site, either through changes in neurotransmitter receptor number, modulation of cable properties, or recruitment of inhibition (Silver, 2010). Because these mechanisms target the postsynaptic membrane, they often modulate overall neuronal excitability and are not input specific. By contrast, neuromodulation of  $P_R$  is intrinsically input specific. Canonically, neuromodulation of  $P_R$  has nonlinear and frequency-dependent effects on synaptic transmission (e.g., parallel changes in facilitation and/or depression, see GABA<sub>B</sub>R in Figure 8). Thus, the ability of D1R to non-canonically suppress  $P_R$  at the presynaptic axon without increasing paired-pulse facilitation represents a novel mechanism for input-specific synaptic gain modulation.

Why do D1Rs suppress synaptic gain, rather than impose a canonical high-pass filter? Cortical neuronal activity is often characterized by sparse and irregular firing patterns (Barth and Poulet, 2012; Boudewijns et al., 2013), with high-frequency bursts encoding behaviorally relevant events (Burgos-Robles et al., 2007; Holmes et al., 2012; Laviolette et al., 2005). Canonical presynaptic neuromodulators like GABA<sub>B</sub>Rs that suppress only low-frequency input are thought to be capable of enhancing the signal-to-noise ratio of these bursts. Conversely, D1R modulation may serve to suppress specific inputs into PFC, independent of input frequency. One major function of dopamine during working memory is to improve the saliency of task-related signals, largely by suppressing activity unrelated to the task at hand in a PKA-dependent manner (Arnsten et al., 1994; Brozoski et al., 1979; Vijayraghavan et al., 2007). Dopamine, by

suppressing glutamatergic activity without altering short-term dynamics, may contribute to this noise suppression. Moreover, we now know that interactions between MDT and PFC are critical for working memory and attentional control (Bolkan et al., 2017; Schmitt et al., 2017). One interesting possibility, highlighted by the input-specific modulation shown here, is that D1Rs functionally enhance the signal-to-noise ratio on MDT inputs by suppressing many other inputs. Thus, the gain modulation employed by dopamine may confer advantages to information processing in PFC, especially during working memory.

## STAR★METHODS

Detailed methods are provided in the online version of this paper and include the following:

- KEY RESOURCES TABLE
- CONTACT FOR REAGENT AND RESOURCE SHARING
- EXPERIMENTAL MODEL AND SUBJECT DETAILS
- METHOD DETAILS
  - Viral Injections
  - Slice Preparation and Whole-Cell Recordings
  - Synaptic Stimulation Experiments and Pharmacology
  - Imaging Experiments
  - Optical Fluctuation Analysis
  - Computational Modeling
  - Short-Term Dynamics in Voltage- and Current-clamp
- QUANTIFICATION AND STATISTICAL ANALYSIS
- DATA AND SOFTWARE AVAILABILITY

## SUPPLEMENTAL INFORMATION

Supplemental Information includes eight figures and one table and can be found with this article online at <https://doi.org/10.1016/j.neuron.2018.07.030>.

## ACKNOWLEDGMENTS

We are grateful to Drs. D. Ron, G. Bouvier, H. Fields, and S. Robinson-Schwartz as well as members of the Bender laboratory for discussions and comments on this work; to Drs. B. Carter and C. Jahr for their support and expertise in designing the optical fluctuation analysis experiments; and to Drs. A. Scimemi and J. Diamond for helpful discussions and sharing simulation code for release models. This research was supported by a scholarship from the ARCS Foundation (K.J. Burke Jr.) and the NIH (DA035913, K.J. Bender).

## AUTHOR CONTRIBUTIONS

Experimental design: K.J. Burke Jr. and K.J. Bender; Experimental execution: K.J. Burke Jr., C.M.K., and K.J. Bender; Data analysis: K.J. Burke Jr., C.M.K., and K.J. Bender; Funding acquisition: K.J. Bender; Project administration: K.J. Burke Jr. and K.J. Bender; Supervision: K.J. Bender; Visualization: K.J. Burke Jr., C.M.K., and K.J. Bender; Writing: K.J. Burke Jr. and K.J. Bender.

## DECLARATION OF INTERESTS

The authors declare no competing interests.

Received: February 6, 2018

Revised: June 3, 2018

Accepted: July 18, 2018

Published: August 16, 2018

## REFERENCES

- Abbott, L.F., and Regehr, W.G. (2004). Synaptic computation. *Nature* 431, 796–803.
- Abbott, L.F., Varela, J.A., Sen, K., and Nelson, S.B. (1997). Synaptic depression and cortical gain control. *Science* 275, 220–224.
- Allbritton, N.L., Meyer, T., and Stryer, L. (1992). Range of messenger action of calcium ion and inositol 1,4,5-trisphosphate. *Science* 258, 1812–1815.
- Arnsten, A.F., Cai, J.X., Murphy, B.L., and Goldman-Rakic, P.S. (1994). Dopamine D1 receptor mechanisms in the cognitive performance of young adult and aged monkeys. *Psychopharmacology (Berl.)* 116, 143–151.
- Barth, A.L., and Poulet, J.F.A. (2012). Experimental evidence for sparse firing in the neocortex. *Trends Neurosci.* 35, 345–355.
- Behr, J., Gloveli, T., Schmitz, D., and Heinemann, U. (2000). Dopamine depresses excitatory synaptic transmission onto rat subiculum neurons via pre-synaptic D1-like dopamine receptors. *J. Neurophysiol.* 84, 112–119.
- Bender, K.J., and Trussell, L.O. (2009). Axon initial segment Ca<sup>2+</sup> channels influence action potential generation and timing. *Neuron* 61, 259–271.
- Bender, K.J., Ford, C.P., and Trussell, L.O. (2010). Dopaminergic modulation of axon initial segment calcium channels regulates action potential initiation. *Neuron* 68, 500–511.
- Betz, W.J. (1970). Depression of transmitter release at the neuromuscular junction of the frog. *J. Physiol.* 206, 629–644.
- Blatow, M., Caputi, A., Burnashev, N., Monyer, H., and Rozov, A. (2003). Ca<sup>2+</sup>-buffer saturation underlies paired pulse facilitation in calbindin-D28k-containing terminals. *Neuron* 38, 79–88.
- Bolkan, S.S., Stujenske, J.M., Parnaudeau, S., Spellman, T.J., Rauffenbart, C., Abbas, A.I., Harris, A.Z., Gordon, J.A., and Kellendonk, C. (2017). Thalamic projections sustain prefrontal activity during working memory maintenance. *Nat. Neurosci.* 20, 987–996.
- Borst, J.G.G., and Sakmann, B. (1998). Calcium current during a single action potential in a large presynaptic terminal of the rat brainstem. *J. Physiol.* 506, 143–157.
- Boudewijns, Z.S.R.M., Groen, M.R., Lodder, B., McMaster, M.T.B., Kalogreades, L., de Haan, R., Narayanan, R.T., Meredith, R.M., Mansvelder, H.D., and de Kock, C.P.J. (2013). Layer-specific high-frequency action potential spiking in the prefrontal cortex of awake rats. *Front. Cell. Neurosci.* 7, 99.
- Branco, T., and Staras, K. (2009). The probability of neurotransmitter release: variability and feedback control at single synapses. *Nat. Rev. Neurosci.* 10, 373–383.
- Brandt, D.S., Coffman, M.D., Falke, J.J., and Knight, J.D. (2012). Hydrophobic contributions to the membrane docking of synaptotagmin 7 C2A domain: mechanistic contrast between isoforms 1 and 7. *Biochemistry* 51, 7654–7664.
- Brenowitz, S.D., and Regehr, W.G. (2007). Reliability and heterogeneity of calcium signaling at single presynaptic boutons of cerebellar granule cells. *J. Neurosci.* 27, 7888–7898.
- Brozoski, T.J., Brown, R.M., Rosvold, H.E., and Goldman, P.S. (1979). Cognitive deficit caused by regional depletion of dopamine in prefrontal cortex of rhesus monkey. *Science* 205, 929–932.
- Bucurenciu, I., Kulik, A., Schwaller, B., Frotscher, M., and Jonas, P. (2008). Nanodomain coupling between Ca<sup>2+</sup> channels and Ca<sup>2+</sup> sensors promotes fast and efficient transmitter release at a cortical GABAergic synapse. *Neuron* 57, 536–545.
- Bucurenciu, I., Bischoffberger, J., and Jonas, P. (2010). A small number of open Ca<sup>2+</sup> channels trigger transmitter release at a central GABAergic synapse. *Nat. Neurosci.* 13, 19–21.
- Burgos-Robles, A., Vidal-Gonzalez, I., Santini, E., and Quirk, G.J. (2007). Consolidation of fear extinction requires NMDA receptor-dependent bursting in the ventromedial prefrontal cortex. *Neuron* 53, 871–880.
- Carter, B.C., and Jahr, C.E. (2016). Postsynaptic, not presynaptic NMDA receptors are required for spike-timing-dependent LTD induction. *Nat. Neurosci.* 19, 1218–1224.

- Chalifoux, J.R., and Carter, A.G. (2011). GABAB receptor modulation of synaptic function. *Curr. Opin. Neurobiol.* 21, 339–344.
- Clarkson, R.L., Liptak, A.T., Gee, S.M., Sohal, V.S., and Bender, K.J. (2017). D3 Receptors Regulate Excitability in a Unique Class of Prefrontal Pyramidal Cells. *J. Neurosci.* 37, 5846–5860.
- Clements, J.D. (1990). A statistical test for demonstrating a presynaptic site of action for a modulator of synaptic amplitude. *J. Neurosci. Methods* 31, 75–88.
- Delaney, A.J., Crane, J.W., and Sah, P. (2007). Noradrenaline modulates transmission at a central synapse by a presynaptic mechanism. *Neuron* 56, 880–892.
- Eggermann, E., Bucurenciu, I., Goswami, S.P., and Jonas, P. (2011). Nanodomain coupling between  $\text{Ca}^{2+}$  channels and sensors of exocytosis at fast mammalian synapses. *Nat. Rev. Neurosci.* 13, 7–21.
- Fedchyshyn, M.J., and Wang, L.-Y. (2005). Developmental transformation of the release modality at the calyx of Held synapse. *J. Neurosci.* 25, 4131–4140.
- Gao, W.-J., and Goldman-Rakic, P.S. (2002). Selective modulation of excitatory and inhibitory microcircuits by dopamine. *Proc. Natl. Acad. Sci. USA* 100, 2836–2841.
- Gao, W.-J., Krimer, L.S., and Goldman-Rakic, P.S. (2001). Presynaptic regulation of recurrent excitation by D1 receptors in prefrontal circuits. *Proc. Natl. Acad. Sci. USA* 98, 295–300.
- Gao, W.-J., Wang, Y., and Goldman-Rakic, P.S. (2003). Dopamine modulation of perisomatic and peridendritic inhibition in prefrontal cortex. *J. Neurosci.* 23, 1622–1630.
- Gee, S., Ellwood, I., Patel, T., Luongo, F., Deisseroth, K., and Sohal, V.S. (2012). Synaptic activity unmasks dopamine D2 receptor modulation of a specific class of layer V pyramidal neurons in prefrontal cortex. *J. Neurosci.* 32, 4959–4971.
- Goutman, J.D., and Glowatzki, E. (2007). Time course and calcium dependence of transmitter release at a single ribbon synapse. *Proc. Natl. Acad. Sci. USA* 104, 16341–16346.
- Hefft, S., Kraushaar, U., Geiger, J.R., and Jonas, P. (2002). Presynaptic short-term depression is maintained during regulation of transmitter release at a GABAergic synapse in rat hippocampus. *J. Physiol.* 539, 201–208.
- Hennig, M.H. (2013). Theoretical models of synaptic short term plasticity. *Front. Comput. Neurosci.* 7, 45.
- Higley, M.J., Soler-Llavina, G.J., and Sabatini, B.L. (2009). Cholinergic modulation of multivesicular release regulates striatal synaptic potency and integration. *Nat. Neurosci.* 12, 1121–1128.
- Hjelmstad, G.O. (2004). Dopamine excites nucleus accumbens neurons through the differential modulation of glutamate and GABA release. *J. Neurosci.* 24, 8621–8628.
- Holmes, A., Fitzgerald, P.J., MacPherson, K.P., DeBrouse, L., Colacicco, G., Flynn, S.M., Masneuf, S., Pleil, K.E., Li, C., Marcinkiewicz, C.A., et al. (2012). Chronic alcohol remodels prefrontal neurons and disrupts NMDAR-mediated fear extinction encoding. *Nat. Neurosci.* 15, 1359–1361.
- Holmes, N.M., Crane, J.W., Tang, M., Fam, J., Westbrook, R.F., and Delaney, A.J. (2017).  $\alpha_2$ -adrenoceptor-mediated inhibition in the central amygdala blocks fear-conditioning. *Sci. Rep.* 7, 11712.
- Huynh, T.G., Cuny, H., Slesinger, P.A., and Adams, D.J. (2015). Novel mechanism of voltage-gated N-type (Cav2.2) calcium channel inhibition revealed through  $\alpha$ -conotoxin Vc1.1 activation of the GABA(B) receptor. *Mol. Pharmacol.* 87, 240–250.
- Jackman, S.L., and Regehr, W.G. (2017). The Mechanisms and Functions of Synaptic Facilitation. *Neuron* 94, 447–464.
- Jackman, S.L., Turecek, J., Belinsky, J.E., and Regehr, W.G. (2016). The calcium sensor synaptotagmin 7 is required for synaptic facilitation. *Nature* 529, 88–91.
- Jarsky, T., Tian, M., and Singer, J.H. (2010). Nanodomain control of exocytosis is responsible for the signaling capability of a retinal ribbon synapse. *J. Neurosci.* 30, 11885–11895.
- Jonas, P., Major, G., and Sakmann, B. (1993). Quantal components of unitary EPSCs at the mossy fibre synapse on CA3 pyramidal cells of rat hippocampus. *J. Physiol.* 472, 615–663.
- Kamiya, H., and Zucker, R.S. (1994). Residual  $\text{Ca}^{2+}$  and short-term synaptic plasticity. *Nature* 371, 603–606.
- Kisilevsky, A.E., Mulligan, S.J., Altier, C., Iftinca, M.C., Varela, D., Tai, C., Chen, L., Hameed, S., Hamid, J., Macvicar, B.A., and Zamponi, G.W. (2008). D1 receptors physically interact with N-type calcium channels to regulate channel distribution and dendritic calcium entry. *Neuron* 58, 557–570.
- Klingauf, J., and Neher, E. (1997). Modeling buffered  $\text{Ca}^{2+}$  diffusion near the membrane: implications for secretion in neuroendocrine cells. *Biophys. J.* 72, 674–690.
- Laviolette, S.R., Lipski, W.J., and Grace, A.A. (2005). A subpopulation of neurons in the medial prefrontal cortex encodes emotional learning with burst and frequency codes through a dopamine D4 receptor-dependent basolateral amygdala input. *J. Neurosci.* 25, 6066–6075.
- Li, L., Bischofberger, J., and Jonas, P. (2007). Differential gating and recruitment of P/Q-, N-, and R-type  $\text{Ca}^{2+}$  channels in hippocampal mossy fiber boutons. *J. Neurosci.* 27, 13420–13429.
- Li, C., Pleil, K.E., Stamatakis, A.M., Busan, S., Vong, L., Lowell, B.B., Stuber, G.D., and Kash, T.L. (2012). Presynaptic inhibition of gamma-aminobutyric acid release in the bed nucleus of the stria terminalis by kappa opioid receptor signaling. *Biol. Psychiatry* 71, 725–732.
- Little, J.P., and Carter, A.G. (2012). Subcellular synaptic connectivity of layer 2 pyramidal neurons in the medial prefrontal cortex. *J. Neurosci.* 32, 12808–12819.
- Luvisetto, S., Fellin, T., Spagnolo, M., Hivert, B., Brust, P.F., Harpold, M.M., Stauderman, K.A., Williams, M.E., and Pietrobon, D. (2004). Modal gating of human CaV2.1 (P/Q-type) calcium channels: I. The slow and the fast gating modes and their modulation by beta subunits. *J. Gen. Physiol.* 124, 445–461.
- Mainen, Z.F., Malinow, R., and Svoboda, K. (1999). Synaptic calcium transients in single spines indicate that NMDA receptors are not saturated. *Nature* 399, 151–155.
- Markram, H., Wang, Y., and Tsodyks, M. (1998). Differential signaling via the same axon of neocortical pyramidal neurons. *Proc. Natl. Acad. Sci. USA* 95, 5323–5328.
- McDonough, S.I., Swartz, K.J., Mintz, I.M., Boland, L.M., and Bean, B.P. (1996). Inhibition of calcium channels in rat central and peripheral neurons by omega-conotoxin MVIIc. *J. Neurosci.* 16, 2612–2623.
- Mintz, I.M., and Bean, B.P. (1993). GABAB receptor inhibition of P-type  $\text{Ca}^{2+}$  channels in central neurons. *Neuron* 10, 889–898.
- Nakamura, Y., Reva, M., and DiGregorio, D.A. (2018). Variations in  $\text{Ca}^{2+}$  Influx Can Alter Chelator-Based Estimates of  $\text{Ca}^{2+}$  Channel-Synaptic Vesicle Coupling Distance. *J. Neurosci.* 38, 3971–3987.
- Naraghi, M., and Neher, E. (1997). Linearized buffered  $\text{Ca}^{2+}$  diffusion in micro-domains and its implications for calculation of  $[\text{Ca}^{2+}]$  at the mouth of a calcium channel. *J. Neurosci.* 17, 6961–6973.
- Neher, E. (1998). Usefulness and limitations of linear approximations to the understanding of  $\text{Ca}^{2+}$  signals. *Cell Calcium* 24, 345–357.
- Oertner, T.G., Sabatini, B.L., Nimchinsky, E.A., and Svoboda, K. (2002). Facilitation at single synapses probed with optical quantal analysis. *Nat. Neurosci.* 5, 657–664.
- Otis, T.S., and Trussell, L.O. (1996). Inhibition of transmitter release shortens the duration of the excitatory synaptic current at a calyceal synapse. *J. Neurophysiol.* 76, 3584–3588.
- Park, D., and Dunlap, K. (1998). Dynamic regulation of calcium influx by G-proteins, action potential waveform, and neuronal firing frequency. *J. Neurosci.* 18, 6757–6766.
- Patil, P.G., de Leon, M., Reed, R.R., Dubel, S., Snutch, T.P., and Yue, D.T. (1996). Elementary events underlying voltage-dependent G-protein inhibition of N-type calcium channels. *Biophys. J.* 71, 2509–2521.

- Patil, P.G., Brody, D.L., and Yue, D.T. (1998). Preferential closed-state inactivation of neuronal calcium channels. *Neuron* 20, 1027–1038.
- Quastel, D.M. (1997). The binomial model in fluctuation analysis of quantal neurotransmitter release. *Biophys. J.* 72, 728–753.
- Rozov, A., Burnashev, N., Sakmann, B., and Neher, E. (2001). Transmitter release modulation by intracellular Ca<sup>2+</sup> buffers in facilitating and depressing nerve terminals of pyramidal cells in layer 2/3 of the rat neocortex indicates a target cell-specific difference in presynaptic calcium dynamics. *J. Physiol.* 531, 807–826.
- Sabatini, B.L., and Svoboda, K. (2000). Analysis of calcium channels in single spines using optical fluctuation analysis. *Nature* 408, 589–593.
- Saviane, C., and Silver, R.A. (2006). Errors in the estimation of the variance: implications for multiple-probability fluctuation analysis. *J. Neurosci. Methods* 153, 250–260.
- Schmitt, L.I., Wimmer, R.D., Nakajima, M., Happ, M., Mofakham, S., and Halassa, M.M. (2017). Thalamic amplification of cortical connectivity sustains attentional control. *Nature* 545, 219–223.
- Scimemi, A., and Diamond, J.S. (2012). The number and organization of Ca<sup>2+</sup> channels in the active zone shapes neurotransmitter release from Schaffer collateral synapses. *J. Neurosci.* 32, 18157–18176.
- Seamans, J.K., and Yang, C.R. (2004). The principal features and mechanisms of dopamine modulation in the prefrontal cortex. *Prog. Neurobiol.* 74, 1–58.
- Seamans, J.K., Durstewitz, D., Christie, B.R., Stevens, C.F., and Sejnowski, T.J. (2001). Dopamine D1/D5 receptor modulation of excitatory synaptic inputs to layer V prefrontal cortex neurons. *Proc. Natl. Acad. Sci. USA* 98, 301–306.
- Seong, H.J., and Carter, A.G. (2012). D1 receptor modulation of action potential firing in a subpopulation of layer 5 pyramidal neurons in the prefrontal cortex. *J. Neurosci.* 32, 10516–10521.
- Sigworth, F.J. (1980). The variance of sodium current fluctuations at the node of Ranvier. *J. Physiol.* 307, 97–129.
- Silver, R.A. (2010). Neuronal arithmetic. *Nat. Rev. Neurosci.* 11, 474–489.
- Sohal, V.S., Zhang, F., Yizhar, O., and Deisseroth, K. (2009). Parvalbumin neurons and gamma rhythms enhance cortical circuit performance. *Nature* 459, 698–702.
- Stanley, E.F. (2016). The Nanophysiology of Fast Transmitter Release. *Trends Neurosci.* 39, 183–197.
- Sugita, S., Shin, O.-H., Han, W., Lao, Y., and Südhof, T.C. (2002). Synaptotagmins form a hierarchy of exocytotic Ca(2+) sensors with distinct Ca(2+) affinities. *EMBO J.* 21, 270–280.
- Surmeier, D.J., Bargiela, J., Hemmings, H.C., Jr., Nairn, A.C., and Greengard, P. (1995). Modulation of calcium currents by a D1 dopaminergic protein kinase/phosphatase cascade in rat neostriatal neurons. *Neuron* 14, 385–397.
- Takahashi, T., Kajikawa, Y., and Tsujimoto, T. (1998). G-Protein-coupled modulation of presynaptic calcium currents and transmitter release by a GABAB receptor. *J. Neurosci.* 18, 3138–3146.
- Tejeda, H.A., Wu, J., Kornspun, A.R., Pignatelli, M., Kashtelyan, V., Krashes, M.J., Lowell, B.B., Carlezon, W.A., Jr., and Bonci, A. (2017). Pathway- and Cell-Specific Kappa-Opioid Receptor Modulation of Excitation-Inhibition Balance Differentially Gates D1 and D2 Accumbens Neuron Activity. *Neuron* 93, 147–163.
- Thévenod, F., and Jones, S.W. (1992). Cadmium block of calcium current in frog sympathetic neurons. *Biophys. J.* 63, 162–168.
- Tritsch, N.X., and Sabatini, B.L. (2012). Dopaminergic modulation of synaptic transmission in cortex and striatum. *Neuron* 76, 33–50.
- Tsodyks, M.V., and Markram, H. (1997). The neural code between neocortical pyramidal neurons depends on neurotransmitter release probability. *Proc. Natl. Acad. Sci. USA* 94, 719–723.
- Urban, N.N., González-Burgos, G., Henze, D.A., Lewis, D.A., and Barrionuevo, G. (2002). Selective reduction by dopamine of excitatory synaptic inputs to pyramidal neurons in primate prefrontal cortex. *J. Physiol.* 539, 707–712.
- Varela, J.A., Sen, K., Gibson, J., Fost, J., Abbott, L.F., and Nelson, S.B. (1997). A quantitative description of short-term plasticity at excitatory synapses in layer 2/3 of rat primary visual cortex. *J. Neurosci.* 17, 7926–7940.
- Vijayraghavan, S., Wang, M., Birnbaum, S.G., Williams, G.V., and Arnsten, A.F.T. (2007). Inverted-U dopamine D1 receptor actions on prefrontal neurons engaged in working memory. *Nat. Neurosci.* 10, 376–384.
- Wang, W., Dever, D., Lowe, J., Storey, G.P., Bhansali, A., Eck, E.K., Nitulescu, I., Weimer, J., and Bamford, N.S. (2012). Regulation of prefrontal excitatory neurotransmission by dopamine in the nucleus accumbens core. *J. Physiol.* 590, 3743–3769.
- Xia, Y., Zhao, Y., Yang, M., Zeng, S., and Shu, Y. (2014). Regulation of action potential waveforms by axonal GABA<sub>A</sub> receptors in cortical pyramidal neurons. *PLoS ONE* 9, e100968.
- Yang, S., Ben-Shalom, R., Ahn, M., Liptak, A.T., van Rijn, R.M., Whistler, J.L., and Bender, K.J. (2016). β-Arrestin-Dependent Dopaminergic Regulation of Calcium Channel Activity in the Axon Initial Segment. *Cell Rep.* 16, 1518–1526.
- Yasuda, R., Sabatini, B.L., and Svoboda, K. (2003). Plasticity of calcium channels in dendritic spines. *Nat. Neurosci.* 6, 948–955.
- Zhang, X.-F., Cooper, D.C., and White, F.J. (2002). Repeated cocaine treatment decreases whole-cell calcium current in rat nucleus accumbens neurons. *J. Pharmacol. Exp. Ther.* 301, 1119–1125.
- Zucker, R.S., and Regehr, W.G. (2002). Short-term synaptic plasticity. *Annu. Rev. Physiol.* 64, 355–405.

**STAR★METHODS****KEY RESOURCES TABLE**

REAGENT or RESOURCE	SOURCE	IDENTIFIER
Antibodies		
Alexa 488 anti-GFP conjugate	Invitrogen	A21311; RRID:AB_221477
Bacterial and Virus Strains		
AAV5-CaMKII $\alpha$ -ChR2-EYFP	UNC Viral Core	N/A
AAV5-Ef1 $\alpha$ -DIO-ChR2-EYFP	UNC Viral Core	N/A
AAV5-hSyn-DIO-gCaMP6f	UPenn Viral Core	N/A
AAV5-Ef1 $\alpha$ -Cre-mCherry	UNC Viral Core	N/A
Chemicals, Peptides, and Recombinant Proteins		
NBQX disodium salt	Tocris	0373
SKF 83822 hydrobromide	Tocris	2075
(R)-Baclofen	Tocris	0796
H89 dihydrochloride	Tocris	29-101-0
(S)-(-)-Sulpiride	Tocris	0895
SCH 23390 hydrochloride	Tocris	0925
(R)-CPP	Tocris	0247
picrotoxin	Tocris	1128
DNQX disodium salt	Tocris	2312
$\omega$ -agatoxin-TK	Peptides international	PAG-4294-s
$\omega$ -conotoxin-MVIIC	Peptides international	PCN-4283-c
$\omega$ -conotoxin-GVIA	Peptides international	PCN-4161-v
Fluo-5F, Pentapotassium Salt, cell impermeant	Invitrogen	F14221
Alexa Fluor 594 hydrazide	Invitrogen	A10438
Alexa Fluor 488 hydrazide	Invitrogen	A10436
Normal Goat Serum	Jackson ImmunoResearch	005-000-121
Prolong Gold Antifade with DAPI	Life Technologies	P36941
Experimental Models: Organisms/Strains		
Mouse: Ai14: 6;129S6-Gt(ROSA)26Sor <sup>tm14(CAG-tdTOMO)Hze</sup> /J	The Jackson Laboratory	JAX: 007908; RRID:IMSR_JAX:007908
Mouse: C57B6J	The Jackson Laboratory	JAX: 000664; RRID:IMSR_JAX:000664
Software and Algorithms		
IGOR Pro	Wavemetrics	RRID: SCR_000325; v6.3
FIJI	<a href="https://fiji.sc/">https://fiji.sc/</a>	RRID: SCR_002285
MATLAB	Mathworks	RRID: SCR_001622; v2016a
Python	<a href="http://python.org">python.org</a>	RRID: SCR_008394; v3.5.2
SciPy	<a href="http://scipy.org">scipy.org</a>	RRID: SCR_008058; v0.18.1
NumPy	<a href="http://numpy.org">numpy.org</a>	RRID: SCR_008633; v1.11.2
Pytest	<a href="http://pytest.org">pytest.org</a>	pytest.org; v3.0
Matplotlib	<a href="http://matplotlib.sourceforge.net">matplotlib.sourceforge.net</a>	RRID: SCR_008624; v2.0.0
Travis CI	Travis CI	<a href="http://travis-ci.com">travis-ci.com</a>
synapseModel	This paper	<a href="https://github.com/kenburke/synapseModel">https://github.com/kenburke/synapseModel</a>
synapseModel Continuous Integration Testing	This paper	<a href="https://travis-ci.org/kenburke/synapseModel">https://travis-ci.org/kenburke/synapseModel</a>

**CONTACT FOR REAGENT AND RESOURCE SHARING**

Further information and requests for resources and reagents should be directed to and will be fulfilled by the Lead Contact, Dr. Kevin Bender ([kevin.bender@ucsf.edu](mailto:kevin.bender@ucsf.edu)).

## EXPERIMENTAL MODEL AND SUBJECT DETAILS

All procedures were performed in accordance with UCSF IACUC guidelines. C57B6 wild type mice or Ai14 reporter mice (Jackson Laboratory, stock no. 007914) aged postnatal day (P) 50-80 were used for all experiments, with the exception of optical fluctuation experiments (Figure 7) where animals from the age range P35-45 were used. No significant differences based on sex were observed, and data were pooled between sexes.

## METHOD DETAILS

### Viral Injections

Subjects were injected with virus at P26-35. Prior to viral injection, mice were anesthetized by isofluorane and head-fixed in a stereotaxic frame. For channelrhodopsin stimulation experiments, subjects were then unilaterally injected with 300-500 nL of AAV5-CamKIIα-hChR2(H134R)-eYFP (“CaMKII-ChR2”) virus into prefrontal cortex (cPFC, from bregma: A/P +1.70, M/L +0.35, D/V -2.60 mm), mediiodorsal thalamus (MD-Thal, from bregma: A/P -1.70, M/L -0.30, D/V -3.45), ventral hippocampus (vHPC, from bregma: A/P -3.30, M/L -3.20, D/V -4.00), orbitofrontal cortex (cOFC, from bregma: A/P +2.2, M/L +1.0, D/V -2.75) and amygdala (Amyg, from bregma: A/P -1.6, M/L -2.75, D/V -5.00). For sparse transfection of local recurrent PFC connections (IPFC), the same coordinates as cPFC were used but instead a virus cocktail was injected including AAV5-EF1α-Cre-IRES-mCherry and AAV5-EF1α-DIO-hChR2(H134R)-eYFP (“Cre-mCherry” and “DIO-ChR2”, ratios between 1:10 and 1:20). For gCaMP experiments, the same injection coordinates and volumes were used in Ai14 heterozygous animals with a viral cocktail that contained a 1:1 ratio of AAV5-hSyn-Flex-gCaMP6f-WPRE-SV40 and Cre-mCherry. Experiments were then performed approximately 4-8 weeks after injection (4-5 weeks cPFC/IPFC/cOFC, 5-6 MD-Thal/Amyg, 6-8 vHPC) to allow sufficient expression and trafficking. Acute slices were prepared from the majority of subjects. Additional subjects were perfused transcardially with 4% paraformaldehyde in phosphate buffered saline (PBS) and coronal sections were prepared (40 μm thickness). Tissue was rinsed with PBS 3 times over the course of 10 min, and then blocked in a solution of PBS with 10% normal goat serum (NGS, Jackson ImmunoResearch) and 0.2% Triton-X in PBS (PBS-T) for 1 hr. Tissue was then incubated in a solution of 2% NGS and 0.1% PBS-T containing an antibody conjugated to a 488 fluorophore (Invitrogen) to amplify the signal from stereotaxic injections of YFP-expressing viruses. This solution was incubated overnight at 4°C, rinsed with PBS 5 times over the course of 20 min, and mounted on slides with ProLong Gold Antifade with DAPI (Life Technologies). Images were obtained using a high speed wide-field microscope (Nikon Ti, with Andor Zyla 5.5 sCMOS) with a 10x/0.45 or 20x/0.75 Plan Apo objectives. Data were post-processed to stitch images and for brightness and contrast in FIJI.

### Slice Preparation and Whole-Cell Recordings

Acute coronal slices of prefrontal cortex (225-300 μm) as well as the injection site if a virus was used (for post-hoc confirmation) were cut in high-sucrose solution, bubbled with 5% CO<sub>2</sub>/95% O<sub>2</sub> and maintained at 4°C. Cutting solution contained (in mM): 87 mM NaCl, 25 mM NaHCO<sub>3</sub>, 25 mM glucose, 75 mM sucrose, 2.5 mM KCl, 1.25 mM NaH<sub>2</sub>PO<sub>4</sub>, 0.5 mM CaCl<sub>2</sub> and 7 mM MgCl<sub>2</sub>. Following cutting, slices were incubated in artificial cerebrospinal fluid (aCSF, see below) for 30 min at 33°C, then at room temperature until recording. Pyramidal cells were visualized with Dodt contrast and two-photon microscopy. Single neurons were identified for electrical recording based on laminar position and teardrop somatic morphology. External aCSF recording solution contained (in mM): 125 NaCl, 2.5 KCl, 1 MgCl<sub>2</sub>, 25 NaHCO<sub>3</sub>, 1.25 NaH<sub>2</sub>PO<sub>4</sub>, 25 glucose; bubbled with 5% CO<sub>2</sub>/95% O<sub>2</sub>; 30-33°C. The day of the experiment, 1.3 mM CaCl<sub>2</sub> and 1 μM sulpiride (D2/3/4 antagonist, Tocris) were added to the aCSF from stock solutions. Recordings were performed in voltage-clamp with glass patch electrodes (2-4 MΩ tip resistance) and internal solution containing (in mM): 113 K-Gluconate, 9 HEPES, 4.5 MgCl<sub>2</sub>, 0.1 EGTA, 14 Tris<sub>2</sub>-phosphocreatine, 4 Na<sub>2</sub>-ATP, 0.3 tris-GTP; ~290 mOsm, pH: 7.2-7.25. Cells were compensated for whole-cell capacitance and series resistance (50%) and voltage-clamped at -80 mV (corrected for 12 mV junction potential) unless otherwise stated. For cesium-based imaging experiments (Figures 2D-2F, QOA), internal solution contained (in mM): 110 CsMeSO<sub>3</sub>, 40 HEPES, 1 KCl, 4 NaCl, 4 Mg-ATP, 10 Na-phosphocreatine, 0.4 Na<sub>2</sub>-GTP, 0.25 Fluo-5F, 0.02 Alexa 594; ~290 mOsm, pH: 7.2-7.25, data corrected for 11 mV junction. Electrophysiological data were acquired at 20 kHz and filtered at 3 kHz using a Multiclamp 700A or 700B amplifier (Molecular Devices) and a custom data acquisition program in Igor Pro (Wavemetrics).

### Synaptic Stimulation Experiments and Pharmacology

For channelrhodopsin stimulation experiments (Figures 1, 2, 4, 5, 8, S1, S2), pairs of blue light stimulation (472 nm LED through 40x objective, 2 x 1 ms at 20 Hz, or more complex patterns in Figure 8) or stimulation via theta stimulating electrode (2 x 200 μs at 20 Hz, Figures 1C and 1E) occurred at regular 15 s intervals to avoid induction of plasticity. Theta simulating electrodes were placed ~100-150 μm lateral to the recording electrode, within layer 5. Light power or electrode amperage were adjusted for each cell to minimize polysynaptic responses, but generally ranged from 0.5 to 2 mW/mm<sup>2</sup> and 0.01-0.2 mA, respectively. Pyramidal cell subtype was identified based on intrinsic excitability during the first 2 min of recording, as described previously (Figure S2, Clarkson et al. 2017). The following criteria were used to exclude cells from data analysis: (1) total temperature range of >1.0°C within one experiment, (2) series resistance (Rs) of >20 MΩ or change in Rs of >20%, (3) holding current ( $I_{hold}$ ) < -100 pA, or change in  $I_{hold}$  > ± 50 pA, (4) change in input resistance ( $R_{in}$ ) > 25%, (5) violation of any of these criteria sooner than 5 min after the last measurement timepoint.

Baseline data began 10 min post-break in (about 7–8 min after start of light stimulation) and lasted for at least 10 min. If a stable baseline EPSC trace was observed, SKF-83822 (D1/D5 agonist, Tocris) was dissolved to 10 mM in ethanol vehicle then immediately (<1 min) diluted in ACSF (20  $\mu$ M) and applied to the slice for 10 min, followed by washout into baseline ACSF. Similar approaches were applied for other pharmacological manipulations, including (*R*)-Baclofen, NBQX, manganese and cadmium, as well as changing extracellular calcium concentration, (distilled H<sub>2</sub>O was used as vehicle for all drugs besides SKF, see Results for concentrations). For PKA blockade experiments (Figure 4), the PKA antagonist H89 was present in all recording solutions (10  $\mu$ M) as well as the incubation chamber for at least 30 min prior to recording. The D1R antagonist SCH was similarly present in all recording solutions for D1R blockade experiments (Figures 1 and 3). For agatoxin TK,  $\omega$ -conotoxin GVIA and  $\omega$ -conotoxin MVIIc (Figures 4 and 6), ACSF was recirculated with the addition of 0.1 mg/mL bovine serum albumin. All drugs were obtained from Tocris Bioscience, with the exception of calcium channel peptide antagonists (agatoxin and  $\omega$ -conotoxin GVIA and MVIIc) and bovine serum albumin, which were obtained from Peptides International and Sigma-Aldrich, respectively.

### Imaging Experiments

For gCaMP experiments, external ACSF also included 50  $\mu$ M picrotoxin, 10  $\mu$ M NBQX or DNQX and 10  $\mu$ M (*R*)-CPP to block GABA-A, AMPA, and NMDA receptors, respectively. AP-evoked bouton gCaMP transients were evoked by a theta-barrel electrode positioned >100  $\mu$ m from imaged boutons. Boutons were identified via two-photon microscopy (910 nm) based on the string-of-pears morphology in the red channel (tdTomato/mCherry expression) and sensitivity of green channel fluorescence to extracellular stimulation (gCaMP expression). A train of three extracellular stimulations (200  $\mu$ s at 20 ms interval) was delivered to evoke bouton-restricted, tetrodotoxin-sensitive gCaMP signals. Approximately 20–30 trials were obtained, followed by application of drug (as with ChR2 stimulation experiments) and another 20–30 trials. Data are displayed as  $\Delta F/F$ , or as peak  $\Delta F/F$  normalized to the baseline mean peak  $\Delta F/F$ .

For imaging of local PFC boutons, K-Gluconate internal solution was used as in ChR2 stimulation experiments, except EGTA was replaced with 250  $\mu$ M Fluo-5F and 20  $\mu$ M Alexa 594. Axons were traced to find an offshoot that contained the string-of-pears morphology, and calcium influx was elicited via precisely timed single action potentials generated by short current injections at the soma (2–2.5 nA  $\times$  2 ms). The same inclusion criteria applied to ChR2 stimulation experiments were applied here, except the holding-current criterion was modified for current-clamp (exclude if membrane voltage ( $V_m$ ) > -63 mV or changed by >  $\pm$  5 mV). Data were always obtained simultaneously from two neighboring boutons to determine whether variability correlated across boutons (see “Optical Fluctuation Analysis”).

For imaging of postsynaptic spines during uncaging experiments (Figure S4) slices were perfused with 3 mM MNI-caged-L-glutamate, and 20  $\mu$ M Alexa 488 was added to the internal solution. Neurons were imaged at 810 nm and MNI-glutamate was uncaged at 720 nm (1 ms pulses, 5–8 mW at focal point). Spines on the basal dendrites within 15  $\mu$ m of the slice surface were chosen for uncaging. EPSC amplitudes were calculated from the average of 5–10 trials before and 10 min after SKF or vehicle application. Paired pulses with modest facilitation were obtained by increasing the laser intensity by 40% on the second pulse.

For imaging of postsynaptic spines during Optical Quantal Analysis experiments (Figures 2D–2F), cells were filled with Cs internal solution containing 250  $\mu$ M Fluo-5F and 20  $\mu$ M Alexa 594. Experiments were done in the presence of 10  $\mu$ M NBQX and 10  $\mu$ M D-Serine. Neurons were voltage-clamped at 0 mV and trains of 5x LED pulses were delivered to the slice in frame-scan mode at 0.06 Hz to locate spines with detectable Ca transients. Due to changes in microscope configuration to allow for simultaneous LED stimulation and imaging, fluorescence was collected on substage detectors only. To avoid damage to our GaAsP PMTs from the LED, a fast physical shutter was inserted in the detection path between the substage periscope and PMT beamsplitter cube housing (Sutter IQ35). Success trials (Figures 2E and 2F) were defined when peak  $\Delta F/F$  exceeded 1, 2, or 3 standard deviations of baseline  $\Delta F/F$  noise within 10 ms of shutter reopening.

### Optical Fluctuation Analysis

Optical fluctuation analysis models calcium influx as a binomial process arising from  $N$  CaVs, each with single-channel current  $i$  and open probability  $p$ . This process is similar to nonstationary fluctuation analysis of electrophysiological recordings, but modified to account for added sources of variability in imaging data that do not reflect variance in channel opening, including dark noise and shot noise. Because variances add linearly, the variance predicted by dark noise and shot noise alone can be subtracted from the measured variance to obtain variance related to CaV activity (Figure 6D):

$$\sigma_{CaV}^2 = \sigma_F^2 - \sigma_d^2 - \sigma_s^2 \quad (\text{Equation 1A})$$

where dark noise,  $\sigma_d^2$ , is the product of the width of the bouton in pixels,  $N_p$ , and the estimated dark noise per pixel,  $\sigma_{d,p}^2$ :

$$\sigma_d^2 = N_p \sigma_{d,p}^2 \quad (\text{Equation 1B})$$

and shot noise,  $\sigma_s^2$ , is the product of the mean change in peak fluorescence,  $\langle \Delta F \rangle$ , and the intensity per photon (in arbitrary units),  $q$ :

$$\sigma_s^2 = q \langle \Delta F \rangle \quad (\text{Equation 1C})$$

The dark-noise parameter,  $\sigma_{d,p}^2$ , was measured in every experiment during the initial 50 ms of each trial (see Figure 6B) by measuring the variance at each pixel over multiple trials and averaging this variance across pixels. The shot-noise parameter  $q$  was estimated by imaging a pipette filled with fluorescein with varying laser intensities and fitting the observed variance to the line:

$$\sigma_F^2 = q\langle F \rangle + \sigma_d^2 \quad (\text{Equation 1D})$$

Once  $q$  and  $\sigma_{d,p}^2$  are measured, the inverse-square of the CaV-related coefficient of variation can then be estimated as:

$$CV_{\text{CaV}}^{-2} = \frac{\langle \Delta F \rangle^2}{\sigma_{\text{CaV}}^2} \quad (\text{Equation 2})$$

One can make quantitative predictions as to how this variance should vary with  $\langle F \rangle$  under different conditions. Specifically,  $CV_{\text{CaV}}^{-2}$  should either reduce linearly, not change, or reduce quickly (nonlinearly, as a “linear rational function”) with reductions in  $N$ ,  $i$ , or  $p$ , respectively:

$$\text{for } \Delta N = R \rightarrow \Delta CV_{\text{CaV}}^{-2} = R \quad (\text{Equation 3})$$

$$\text{for } \Delta i = R \rightarrow \Delta CV_{\text{CaV}}^{-2} = 1 \quad (\text{Equation 4})$$

$$\text{for } \Delta p = R \rightarrow \Delta CV_{\text{CaV}}^{-2} = \frac{R(1 - k)}{1 - kR} \quad (\text{Equation 5})$$

where  $R = \langle F_{\text{post}} \rangle / \langle F_{\text{baseline}} \rangle$  and  $k = p_{\text{baseline}}$ .

To ensure that variance was related to fluctuations in CaV activity, care was taken to minimize other sources of variance, including optical drift. Data were excluded if: (1) the timing of the action potential peak changed by > 0.1 ms, (2) trial-by-trial variability in peak ΔG/R after the AP was correlated when monitored between two simultaneously imaged boutons in series, or (3) failures were observed in both boutons within the same trial, as these effects could result from AP conduction failures rather than independent CaV opening failures. Furthermore, time-locked vehicle controls showed no rundown of more than 5% up to 100 trials, after which spontaneous rundown of peak ΔG/R was occasionally observed; therefore, all OFA experiments were limited to a maximum of 100 trials, and variance was estimated with trial-to-trial correction for drift:

$$\sigma_F^2 = \frac{1}{2(n-1)} \sum_{i=1}^{n-1} (\Delta F_{i+1} - \Delta F_i)^2 \quad (\text{Equation 6})$$

where  $n$  is the number of trials. This is equivalent to the standard measurement of variance as the sum of squared difference from the mean for an experiment without systematic drift, but has the advantage of minimizing unwanted increases in variance due to runup or rundown.

### Computational Modeling

All modeling was performed in Python 3.5 (Numpy version 1.11). Images in Figure 7 were generated using Matplotlib version 2.0. See Table S1 for a comprehensive list of model parameters in all models. Models were subjected to continuous integration testing using pytest via Travis CI (<https://travis-ci.org/kenburke/synapseModel>) to ensure successful execution across a wide range of combinations of parameter values, including rejection of invalid parameters (e.g., negative channel open probabilities or trial numbers).

We first designed a reduced computational model of synaptic transmission in order to directly incorporate the binomial parameters obtained from optical fluctuation analysis. We simulated 50 presynaptic axons, where calcium influx in response to each simulated action potential was modeled as the result of a binomial process resulting from  $N$  CaVs, each with independent probability  $p$  of increasing the calcium concentration instantaneously by amount  $i$  (in arbitrary units). Calcium concentration decayed with a single-exponential time course (time constant = 50 ms, fit alongside Hill function to produce modest paired-pulse facilitation, Brenowitz and Regehr, 2007). We simulated the stochastic opening of single CaVs using a Monte Carlo method by generating an array of random uniformly distributed numbers in the range [0, 1] and testing whether the generated numbers were less than the open probability  $p$  on any given trial. Total calcium concentration was then calculated as the sum of all successful CaV openings ( $i$  current each) and residual calcium present from previous APs.

Vesicle release probability ( $P_R$ ) was then calculated per synapse as a Hill function of the calcium concentration (when zero CaVs opened in response to a stimulus,  $P_R$  was set to zero to prevent release purely due to residual calcium). The maximum  $P_R$  per vesicle was a parameter that we hand-tuned in order to obtain realistic values of  $P_R$  (see Table S1, “vesicle\_prox”). Individual release events were then modeled using a Monte Carlo method akin to CaV channel openings. Total quantal content was calculated as the total number of successful vesicle release events across synapses for a single trial. Quantal content was convolved with an AMPA-like waveform (kinetics adapted from Jonas et al., 1993) for visualization purposes only, as we wanted to avoid the contribution of post-synaptic filtering in our estimation of neurotransmitter release statistics.

This process was repeated 10,000 times for each parameter set tested. Modulation of individual model parameters (e.g.,  $i_{CaV}$  or  $p_{open}$ ) repeated this array of 10,000 simulations for a range of parameter values, scaling the parameter from 20% to 100% of its baseline value in 5% increments. In order to make fair comparisons between presynaptic configurations with differing numbers of CaVs driving release, we held constant the expected average calcium influx (the product  $N_{CaV} \cdot i_{CaV} \cdot p_{open}$ ). This was achieved by multiplying the number of CaVs and dividing the single-channel current by the same parameter, “num\_cav\_ratio” (see Table S1). PPR and  $CV^{-2}$  were calculated using the quantal content rather than the peak AMPA current for computational efficiency because they were mathematically equivalent. Simulation runs were then saved in a.pkl format for subsequent reference and replication.

In a second simulation, we modeled the diffusion of calcium from CaVs to vesicles explicitly using the “linearized buffer approximation” (Naraghi and Neher, 1997; Neher, 1998):

$$[Ca^{2+}] = \frac{i_{CaV}}{4\pi FD_{Ca}r} \exp\left(\frac{-r}{\lambda}\right) \quad (\text{Equation 7A})$$

where  $i_{CaV} = 0.13 \text{ pA}$  (Li et al., 2007; Scimemi and Diamond, 2012),  $F$  is the Faraday constant,  $D_{Ca}$  is the diffusion coefficient of free calcium ( $220 \mu\text{m}^2/\text{s}$ , Allbritton et al., 1992),  $r$  is the distance between the vesicle and the calcium influx, and  $\lambda$  is the characteristic length constant:

$$\lambda = \sqrt{\frac{D_{Ca}}{K_{on}[B]_{free}}} \quad (\text{Equation 7B})$$

where  $K_{on}$  is the rate of calcium binding to free buffer (Klingauf and Neher, 1997) and  $[B]_{free}$  is the concentration of free buffer:

$$[B]_{free} = \frac{[B]_{total}K_D}{K_D + [Ca]_{basal}} \quad (\text{Equation 7C})$$

where  $[B]_{total}$  is the total concentration of endogenous buffer,  $K_D$  is the buffer dissociation constant and  $[Ca^{2+}]_{basal}$  is the basal free calcium concentration. Taken together, these three equations allowed us to calculate the initial calcium concentration as a function of distance from the point of calcium influx (assuming rapid equilibration at short distances). The calcium concentration then decayed exponentially, independent of distance, with a time constant of 40 ms to mimic slower timescale extrusion mechanisms (Brenowitz and Regehr, 2007).

The second feature we added to this model was two Hill functions with realistic parameters for calcium affinity and cooperativity to mediate vesicle release and facilitation. The Hill parameters for both functions were adapted from electrophysiological as well as biochemical measurements of affinity and cooperativity for synaptotagmin1 and synaptotagmin7 (Brandt et al., 2012; Scimemi and Diamond, 2012; Sugita et al., 2002). The initial release probability  $p_{release}$  was calculated by the first, lower affinity Hill function using instantaneous initial calcium concentration immediately following the AP, which was then facilitated based on the residual calcium concentration preceding the AP via the second Hill function:

$$p_{release} = Hill_{release}([Ca]) \cdot (1 + Hill_{facil}([Ca])) \quad (\text{Equation 8A})$$

where

$$Hill([Ca]) = \frac{S \cdot [Ca]^N}{EC_{50}^N + [Ca]^N} \quad (\text{Equation 8B})$$

and  $S$ ,  $N$ , and  $EC_{50}$  are parameters for maximum value, cooperativity, and half-maximal effective concentration, respectively. The values for cooperativity and half-maximal effective concentration were obtained from the literature (see Table S1), and the maximum value parameter  $S$  for the release and facilitation Hill functions was tuned to reproduce a realistic baseline release probability (based on OQA data, Figure 2) and modest baseline paired-pulse facilitation, respectively.

In the initial reduced model, the increase in PPR with reductions in  $i_{CaV}$  was the result of both release events being calculated with a single Hill function. With the addition of a second, higher affinity Hill function to mediate facilitation, it was necessary to incorporate vesicle depletion and replenishment parameters to account for the increases in paired-pulse facilitation observed with reductions in  $i_{CaV}$  (Abbott et al., 1997; Scimemi and Diamond, 2012; Tsodyks and Markram, 1997). Each “synapse” was paired with one vesicle (because synapses are independent in this model, one could equivalently conceptualize them as independent pairs of release sites and CaV clusters). At the beginning of each trial, it was assumed that all vesicles were replenished and available for release by defining a binary variable *pool\_size*. After calculating calcium influx and stochastic release for the first AP, the variable *pool\_size* was set to zero at synapses where release was successful. On the second AP, all synapses where *pool\_size* = 0 were randomly “replenished” (i.e., *pool\_size* set to 1) with a time-dependent probability:

$$Pr_{recov} = 1 - \exp\left(\frac{-t}{\tau_{recov}}\right) \quad (\text{Equation 9A})$$

where  $t$  is the time elapsed since the previous AP (i.e., the inter-stimulus interval), and  $\tau_{recov}$  is the replenishment time constant. After determining if each empty release site was replenished, the release probability for the second AP was calculated as

$$p_{corrected} = pool\_size \cdot p_{release} \quad (\text{Equation 9B})$$

where  $p_{release}$  is the output of [Equation 8A](#).

In the reduced model of [Figure 7](#), when increasing the number of CaVs per synapse we reduced the single channel current in order to maintain constant the expected calcium concentration per synapse. Because we used realistic values for CaV single-channel current in the diffusion model, when increasing the number of channels per synapse we instead kept single-channel current constant and simply increased the CaV-vesicle distance to keep the expected value of the calcium concentration constant at each synapse ([Figures S7F and S7I](#)). Without this adjustment, release probability would quickly saturate due to the Hill Function nonlinearity with the addition of even one CaV (data not shown, but see [Figure S7G](#)). The following values for CaV-vesicle distance were used for synapses with the corresponding number of CaVs:

Number CaVs	CaV-Vesicle Distance (nanometers)
1	15
2	23.3
3	29.2
5	37.6
10	50.7
50	86.2

In some simulations, facilitation was modeled phenomenologically ([Figure S6](#)). In these simulations, we began with the reduced model from [Figure 7](#), but rather than modeling exponential decay of calcium concentration, the vesicle release probability was calculated directly from the calcium influx per AP. The release probability for the second AP was then scaled according to the following formula:

$$p_{release} = p_{initial}(1 + ks(1 - p_{initial})) \quad (\text{Equation 10A})$$

where  $p_{initial}$  is the initial release probability calculated from the Hill function of the calcium concentration,  $k$  is the facilitation parameter (“phenom\_param,” [Table S1](#)) and:

$$s = \begin{cases} 1, & \geq 1 \text{ CaV opening previous AP} \\ 0, & \text{otherwise} \end{cases} \quad (\text{Equation 10B})$$

### Short-Term Dynamics in Voltage- and Current-clamp

Evaluation of short-term plasticity for longer trains of stimuli and across different frequencies was achieved using the same preparation as earlier ChR2 stimulation experiments but with custom stimulation patterns ([Figure 8](#)). In order to quantify the relative suppression of ongoing activity relative to single EPSCs, we quantified the charge ratio:

$$R_Q = \frac{Q_T}{Amp_1} \quad (\text{Equation 11A})$$

where

$$Q_T = \frac{\text{Total Charge}_{post}}{\text{Total Charge}_{baseline}} \quad (\text{Equation 11B})$$

$$Amp_1 = \frac{\text{First Amplitude}_{post}}{\text{First Amplitude}_{baseline}} \quad (\text{Equation 11C})$$

For current-clamp experiments ([Figure 8](#)), EPSP amplitude was monitored by stimulating once 250 ms before the onset of injected noisy current waveforms. In each cell, rheobase was estimated by injecting one-second long square pulses of current in 25 pA increments until at least one AP was evoked. The noise stimulus was generated by simulating EPSCs at 1,000 Hz as the product of two exponentials, with amplitude +25 pA and rise/decay time constants of 0.303/2.0 ms ([Sohal et al., 2009](#)). IPSCs were similarly generated, but with amplitude -25 pA at 250 Hz. The noisy current stimulus was then added to a square pulse of amplitude (rheobase - 50 pA), as the mean of the noisy current stimulus was ~50 pA. Following an initial LED pulse 500 ms after the onset of the noisy-current waveform, intervals corresponding to 1, 5, 10, and 20 Hz were shuffled, generating a train of LED stimuli of varying frequency. Pairs of trials with the same noisy current waveform were interleaved with and without LED stimulation (data not shown). After collecting baseline data, D1R and GABA<sub>B</sub>R agonists were bath-applied for 10 min before collecting the “post-drug” data.

Offline, spikes were detected reliably by crossing 0 mV and LED-triggered averages of instantaneous frequency were calculated using 3 ms bins. The change in evoked spiking quantified in [Figure 8J](#) measured average instantaneous frequency in the 12 ms following an LED pulse. The same inclusion criteria were used for these experiments as outlined for ChR2 oEPSC experiments.

#### QUANTIFICATION AND STATISTICAL ANALYSIS

All data are shown as mean  $\pm$  SEM, where “n” refers to the number of cells (for electrophysiological recording experiments) or boutons or spines (for Ca imaging experiments). Summary data and the name and results of statistical tests are interspersed with text in parentheticals in the Results section. Preliminary analysis and data visualization was performed in Igor Pro and MATLAB (MathWorks). Statistical tests used Kruskal-Wallis with Wilcoxon’s rank-sum test and the Holm-Sidak correction for multiple comparisons. Significance was set to  $p < 0.05$  unless otherwise stated.

#### DATA AND SOFTWARE AVAILABILITY

All code for computational models of vesicle release, and tutorials for simple simulations or replication, is available at <https://github.com/kenburke/synapseModel>.